

AD-A083 343

MCDONNELL DOUGLAS ASTRONAUTICS CO HUNTINGTON BEACH CA  
SELF-CONSISTENT NUCLEAR PARTICLE AND FIELD STUDIES.(U)  
OCT 79 G J MROZ, W P OLSON, K A PFITZER

F/G 20/9

DNA001-77-C-0240

UNCLASSIFIED

DNA-4830F

NL

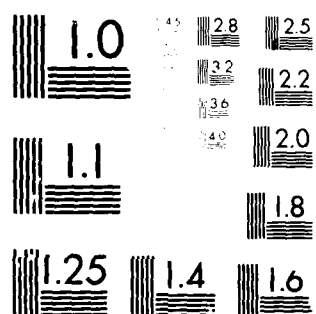
[ OF ]  
AD  
AC 30343

END

DATE

FILED

DTIC



MICROCOPY RESOLUTION TEST CHART  
NATIONAL BUREAU OF STANDARDS-1963-A

(12) **LEVEL** III  
NW

AP-E 300 734

DNA 4830F

ADA 083343

## SELF-CONSISTENT NUCLEAR PARTICLE AND FIELD STUDIES

G. J. Mroz  
W. P. Olson  
K. A. Pfitzer  
S. Schneider  
McDonnell Douglas Corporation  
5301 Bolsa Avenue  
Huntington Beach, California 92647

1 October 1979

Final Report for Period April 1977—March 1979

CONTRACT No. DNA 001-77-C-0240

APPROVED FOR PUBLIC RELEASE;  
DISTRIBUTION UNLIMITED.

DTIC  
ELECTE  
S APR 24 1980 D  
B

THIS WORK SPONSORED BY THE DEFENSE NUCLEAR AGENCY  
UNDER RDT&E RMSS CODE B322077464 S99QAXHC06607 H2590D.

Prepared for  
Director  
DEFENSE NUCLEAR AGENCY  
Washington, D. C. 20305

80 3 13 016

Destroy this report when it is no longer  
needed. Do not return to sender.

PLEASE NOTIFY THE DEFENSE NUCLEAR AGENCY,  
ATTN: STTI, WASHINGTON, D.C. 20305, IF  
YOUR ADDRESS IS INCORRECT, IF YOU WISH TO  
BE DELETED FROM THE DISTRIBUTION LIST, OR  
IF THE ADDRESSEE IS NO LONGER EMPLOYED BY  
YOUR ORGANIZATION.



UNCLASSIFIED

SECURITY CLASSIFICATION OF THIS PAGE (When Data Entered)

REPORT DOCUMENTATION PAGE		READ INSTRUCTIONS BEFORE COMPLETING FORM
1. REPORT NUMBER DNA 4830F	2. GOVT ACCESSION NO. AD-A083 343	3. RECIPIENT'S CATALOG NUMBER
4. TITLE (and Subtitle) SELF-CONSISTENT NUCLEAR PARTICLE AND FIELD STUDIES		5. TYPE OF REPORT & PERIOD COVERED Final Report for Period April 1977—March 1979
7. AUTHOR(s) G. J. Mroz W. P. Olson		6. PERFORMING ORG. REPORT NUMBER
K. A. Pfitzer S. Schneider		8. CONTRACT OR GRANT NUMBER(s) DNA 001-77-C-0240 <i>new</i>
9. PERFORMING ORGANIZATION NAME AND ADDRESS McDonnell Douglas Corporation 5301 Bolsa Avenue Huntington Beach, California 92647		10. PROGRAM ELEMENT, PROJECT, TASK AREA & WORK UNIT NUMBERS Subtask S99QAXHC066-07
11. CONTROLLING OFFICE NAME AND ADDRESS Director Defense Nuclear Agency Washington, D.C. 20305		12. REPORT DATE 1 October 1979
14. MONITORING AGENCY NAME & ADDRESS (if different from Controlling Office)		13. NUMBER OF PAGES 92
		15. SECURITY CLASS (of this report) UNCLASSIFIED
		15a. DECLASSIFICATION/DOWNGRADING SCHEDULE
16. DISTRIBUTION STATEMENT (of this Report)  Approved for public release; distribution unlimited.		
17. DISTRIBUTION STATEMENT (of the abstract entered in Block 20, if different from Report)		
18. SUPPLEMENTARY NOTES  This work sponsored by the Defense Nuclear Agency under RDT&E RMSS Code B322077464 S99QAXHC06607 H2590D.		
19. KEY WORDS (Continue on reverse side if necessary and identify by block number) Plume                      Atmosphere                      Magnetic Signature                      Induction Fields Striations                      High Altitude                      Electric Field Nuclear Burst                      MICE                      Magnetic Field Magnetosphere                      MELT                      Plasma		
20. ABSTRACT (Continue on reverse side if necessary and identify by block number) The objectives of this study were to approach the problem of plasmas arti- ficially injected into the high altitude ionosphere from the viewpoint of their interaction with the ambient electromagnetic field environment (e.g., those associated with the magnetospheric substorm and the daily wobble of the earth's dipole magnetic field) and in a self-consistent manner to examine the mutual influence of the plasma and the electromagnetic field. It was found that the natural electric fields contribute to both the drift motion and structuring of the plasma. To do this, the principal sources of the natural		

DD FORM 1473  
1 JAN 73

EDITION OF 1 NOV 65 IS OBSOLETE

UNCLASSIFIED

SECURITY CLASSIFICATION OF THIS PAGE (When Data Entered)

UNCLASSIFIED

SECURITY CLASSIFICATION OF THIS PAGE(When Data Entered)

20. ABSTRACT (Continued)

electric field were identified, and a model of the most persistent field (resulting from the daily variation of the magnetospheric magnetic field) was developed. The model describes the total electric field which includes a component produced by the plasma as it responds to the field induced by the wobbling dipole.

The natural electric fields in the magnetosphere have periods of the order of 0.25 hour, or more, and are thus very low frequency in character. As a result they penetrate the plasmas of interest here with very little loss of energy (i.e., have large skin depths). The estimates of plasma properties were performed under several simplifying assumptions; the range of values used are typical of the cases of interest to this study. The dominant feature of the problem is the extremely low frequency range of the electromagnetic waves. The normal variations of the other parameters (such as the collision frequencies) with respect to the values used in the present work do not alter the conclusions appreciably.

In addition to developing the electric field model itself, the possible influence of this electric field on the motion and structure of an artificially generated plasma was investigated. Although preliminary in nature the results of these calculations indicate that the plasma can be influenced by this field; the  $\vec{E} \times \vec{B}$  drift not only contributes to the general motion of the plasma but can also influence internal structuring of the plasma. High density plasmas in the ionosphere are expected to be influenced only slightly by the smaller natural electric field there. As these plasmas expand outward along magnetic field lines, the penetration of the field increases and the decrease in  $B$  ( $\vec{E} \times \vec{B}/B^2$  increases) produces a significant plasma drift velocity. The penetration of  $\vec{E}$  is anisotropic in nature and depends on the detailed structure of the plasma. The plasma is expected to drift with respect to the magnetic field lines, the variation in drift velocities throughout this region contributing to the internal structuring of the plasma.

The conditions in the plasma which allow penetration of the external electric field are also those under which the assumption that magnetic field lines are essentially equipotentials becomes poor. The breakdown of this condition allows the less dense plasmas, in the extended region of the magnetically contained plasma plume, to act more or less independently of the denser, low altitude regions. Models of plasma dynamics in the magnetosphere which depend on the "field line coupling" assumption cannot correctly describe plasma motions in the regime of interest here.

Work was also performed on the perturbations to the ambient fields resulting from the presence of the artificial plasma. The result is the evaluation of the magnetic signatures which could be observed by earth based magnetometer stations. The results for a model high altitude nuclear weapon burst are compared with the available data. They are positive and indicate that this technique can be useful in the evaluation of the performance of hydrodynamic codes such as MICE and MELT. Further extension of these techniques to evaluate the effects of high altitude nuclear weapon detonations on the magnetosphere may prove very useful in studies of communication, satellite, and ballistic missile defense system performance under nuclear attack. Multiple burst effects is one area where this technique could be applied. Also the techniques used for quantitatively determining induced electric fields can be extended for use in the auroral regions and to higher latitudes generally and can be applied to the multiburst environment.

UNCLASSIFIED

SECURITY CLASSIFICATION OF THIS PAGE(When Data Entered)

## TABLE OF CONTENTS

<u>Section</u>		<u>Page</u>
1	INTRODUCTION - - - - -	5
2	OBSERVED ELECTROMAGNETIC ENVIRONMENT - - - - -	9
3	ELECTROMAGNETIC FIELDS - - - - -	15
	3.1 The Magnetic Field Model - - - - -	15
	3.2 The Electric Field Model - - - - -	20
	3.3 Extensions of the Models - - - - -	37
4	INTERACTION OF ARTIFICIALLY PRODUCED PLASMA - - - - WITH NATURAL FIELDS	39
	4.1 Structure and Motion of Artificial - - - - Plasma with Natural Fields	39
	4.1.1 Plasma Characteristics in a Low - - - Frequency Field	39
	4.1.2 Plasma Behavior in a Low Frequency - - Field	45
	4.2 Perturbation of the Natural Field by the - - Artificial Plasma	50
	4.2.1 Magnetic Signatures - - - - -	50
	4.2.2 Multiburst Effects - - - - -	63
5	CONCLUSIONS AND RECOMMENDATIONS - - - - -	65
	References - - - - -	68
 <u>Appendices</u>		
A	DERIVATION OF PLASMA CHARACTERISTICS IN AN EXTERNAL MAGNETIC FIELD	A-1
B	DERIVATION OF PLASMA DRIFT VELOCITIES	B-1
C	CURRENT DENSITY MAGNETIC TAPE FORMAT	C-1
D	DERIVATION OF LAGRANGEAN VOLUME ELEMENT	D-1

# LIST OF ILLUSTRATIONS

<u>Figure</u>		<u>Page</u>
3-1	Three-dimensional View of the Current System for Tilt = 0°	17
3-2	Field Lines in the Noon-Midnight Meridian Plane	19
3-3	Optical Tracking Data of the Barium Clouds	21
3-4	Earth Intercept of Field Lines for Geosynchronous Orbit	22
3-5	Potential, Uniform Bound Day = 172, UT = 0, 6, 12, 18	28
3-6	Potential, R,M,SPH Bound Day = 172, UT = 0, 6, 12, 18	29
3-7	Total Electric Field Experienced by a Charged Particle Rotating with the Earth at Synchronous Orbit	31
3-8	Total Electric Field Experienced by a Charged Particle Rotating with Earth at Synchronous Orbit	32
3-9	/E/ In Rotating Frame	33
3-10	/E/ In Inertial Frame	34
3-11	Time Rate of Change of Proton Kinetic Energy, Guiding Center Motion Contribution (UT = 16.6 Hrs, Day = 172, Equatorial Plane, Longitude = 0°)	35
3-12	Time Rate of Change of Proton Kinetic Energy Due to Rotation About the Guiding Center (UT = 16.6, Day = 172, Equatorial Plane, Longitude = 0°)	36
3-13	Field Line Originating at 72° magnetic Latitude for Varying Strengths of the Tail Field	38
4-1	Geometrical Dependence of Penetrating Tangential Component of $\vec{E}$	47
4-2	Geometrical Dependence of $\vec{E} \times \vec{B} / B^2$	51
4-3	Observed Starfish Magnetic Field	52
4-4	Currents Flowing with a Typical 4 Megaton Plume	54
4-5	Currents Flowing with a Typical 4 Megaton Plume	55
4-6	Currents Flowing with a Typical 4 Megaton Plume	56



# LIST OF ILLUSTRATIONS

<u>Figure</u>		<u>Page</u>
4-7	The ( $\alpha, \beta$ ) Coordinates for the Field-Aligned Dipole Coordinate System Far from the Earth	59
D-1	The ( $\alpha, \beta$ ) Coordinates for the Field-Aligned Dipole Coordinate System Far from the Earth	D-3

ACCESSION for		
NTIS	White Section	<input checked="" type="checkbox"/>
DDC	Buff Section	<input type="checkbox"/>
UNANNOUNCED		<input type="checkbox"/>
JUSTIFICATION _____		
BY _____		
DISTRIBUTION/AVAILABILITY CODES		
Dist.	AVAIL	and/or SPECIAL
A		

## Section 1 INTRODUCTION

This is the final report of a study performed at McDonnell Douglas Astronautics Company (MDAC) under contract with the Defense Nuclear Agency (DNA). MDAC performed the following tasks enumerated in the contract work statement:

1. Provide quantitative information on the earth's naturally occurring space environment as requested by DNA or members of the High Altitude Nuclear Effects Working Group.
2. Quantitatively determine the total electric field, in the presence of a plasma, induced by a naturally occurring time varying magnetic field.
3. Assess quantitatively the importance of this electric field on the motions of plasmas artificially injected into the geomagnetic field.

During the contract effort representatives from MDAC also attended several phenomenology working group meetings and met several times with the DNA contract monitor. Detailed exchanges of technical information were also held between the MDAC group working on this contract with several members of the Mission Research Corporation (MRC) organization associated with the running of the hydrodynamic codes MICE and MELT.

From these discussions it became apparent that any technique which could be used to verify the validity of these high altitude hydrodynamic calculations would be of interest to DNA. As a result, work not included in the contract work statement was performed in an attempt to quantitatively model the magnetic signature of a high altitude burst.

Techniques developed at MDAC, used in generating models of the magnetospheric magnetic field, were applied to the internal current systems of high altitude artificially produced plasmas to calculate their magnetic

signatures at any location in and around the plasmas. Preliminary results are included in this report. The plasma plume model and internal current distributions used in these calculations were obtained from MRC and result from calculations performed by them with the MICE/MELT code. We recommend that similar calculations be performed by MRC for actual weapon test events and the MDAC procedures can then be used to compare model results with the observed perturbations of the geomagnetic field. This is a straightforward and available way to test the accuracy of the late time hydrodynamic codes.

Included in this report is a brief description of the magnetosphere, emphasizing those features which may have a direct bearing on artificially produced, high altitude plasmas. A brief description of a time dependent model of the earth's external magnetic field developed at MDAC is also provided. The induced electric field associated with the model magnetic field is also described. It is given in terms of the time varying magnetic vector potential and is used to quantitatively assess the penetration and persistence of the naturally occurring electric field in a dense plasma. The techniques used to generate the magnetic induction vector,  $\vec{B}$ , in the magnetic field model and the vector magnetic potential,  $\vec{A}$ , used to calculate the electric field are both described. These techniques were modified and applied to the calculations of magnetic signatures of high altitude artificial plasma.

The magnetospheric electric field model presented in this report represents only those fields which results from the daily wobble of the geomagnetic dipole. Other naturally occurring electric fields are much larger in magnitude but are more limited in extent and/or duration. The particular choice of induced electric field made for this study was primarily dictated by the availability of a quantitative model of both  $\vec{B}$  and  $\vec{A}$  caused by the wobbling dipole.

The latest MDAC magnetic field model (also described here) is sufficiently flexible to include fluctuations in the magnetic field resulting from any variations in the magnetospheric current system. It is capable of modeling magnetic substorm activity and any other perturbations of the magnetospheric fields resulting from changes in the strengths

and topologies of the current systems. High altitude nuclear weapon detonations (such as those occurring at satellite altitudes) can also perturb the magnetospheric current systems and be responsible for large scale fluctuations in the earth's magnetic field. The energy deposited in this system may produce subsequent substorm activity. The techniques, used to model the general time varying behavior of the naturally occurring electromagnetic field, can be extended for use in determining the total environment in a multiburst scenario. (It has already been used to study burst magnetic signatures as is discussed in this report.)

In the sections of this report dedicated to assessing the interaction of artificially produced plasmas with the natural magnetospheric fields, several aspects of this interaction are investigated. Of principal concern to this study was the interaction of the electric field with the plasma and the resulting plasma structuring and motion. This was investigated for the case of the electric field induced by the diurnal variation of the magnetic field. Various regimes for this plasma are identified where even this rather weak electric field can have a significant effect on plasma structuring and motion. Fields which result from other naturally occurring sources are also expected to be significant in this respect but have not yet been quantitatively examined.

## Section 2

### OBSERVED ELECTROMAGNETIC ENVIRONMENT

In order to properly describe the structure of the plume and the motion of low energy plasma during late times, it is necessary to understand the natural plume environment in the earth's ionosphere and magnetosphere. In this section the particle and field properties of these regions are briefly described with attention given to the electromagnetic field.

The earth's magnetosphere is formed and maintained by the interaction of the earth's magnetic field with the solar wind. The solar wind is a neutral plasma whose velocity (in an earth reference frame) varies from about 300 to 1000 km/sec and whose density of ion-electron pairs varies from 0.1 to several hundred per cubic centimeter. The solar wind carries with it a magnetic field which is seen, when transformed into an earth reference system, as both a magnetic and electric field. Because of the highly variable nature of the solar wind, the magnetosphere exhibits both "quiet" and "disturbed" topologies.

The total magnetospheric magnetic field is important in the quantitative description of the nuclear burst in several ways. First the burst particles must expand against the pressure of the magnetic field. Later the magnetic field topology determines the range over which the low energy charged particles move and also the location of the conjugate region.

The earth's main magnetic field exhibits only a secular variation and for the nuclear plume problem can be represented as constant in time. Also, for most applications it suffices to represent the main field as a dipole with a pole strength of  $0.314 \text{ gauss times } R_E^3$  ( $R_E$  = earth radii). This dipole is placed at the center of the earth with an inclination of  $11.7^\circ$  to the earth's rotation axes and lying in the meridian plane  $69^\circ$  west of Greenwich. For the accurate calculation of the field in the vicinity of the earth it is sometimes necessary to use a more complex representation of the

main field. Such descriptions are available as spherical harmonic expansions. Such representations may be necessary to accurately describe particle and field behavior at a particular point in space and also to determine the motions of charged particles and locations of magnetic conjugate regions.

The formation of the magnetosphere by the dipole - solar wind interaction is caused mainly by the magnetopause current system. These currents are formed by the deflections of the solar wind plasma by the geomagnetic dipole. (Since the solar wind electrons and protons are deflected in opposite directions, they form a current system.) These currents grossly distort the magnetic field within the magnetosphere and simultaneously limit the penetration of the solar wind. The region over which these currents flow is called the magnetopause - the boundary of the magnetosphere. Thus, the magnetosphere may be thought of as that region of space where the earth's magnetic field persists.

Two other current systems flow in the magnetosphere which also grossly influence magnetic field topology. In the inner magnetosphere where the field geometry remains essentially dipolar, charged particles can remain "trapped" for long periods of time. Since the particle motions are charge dependent, a torroidal current system, the so-called ring current, is formed. In the antisolar region (the "tail" of the magnetosphere) currents flow across the equatorial region much the same way they did in the ring current except that they are not permanently trapped but flow in and out of the tail along its flanks.

In order to properly describe the interaction of the plume during late times, it is necessary to describe the total magnetic field produced by the earth's main field and the fields from these magnetospheric current systems. Near the earth's surface, of course, the main field dominates and it may not be necessary to consider the magnetospheric contribution. However, at geosynchronous altitude, the magnetospheric currents produce a large portion of the total field. For L values larger than 4 it is generally necessary to consider the magnetospheric contributions. (The L value is the

distance of the farthest extent of the field line from the center of the earth measured in earth radii. Thus, the L value of field lines through geosynchronous orbit is about 6.6.)

Although the main field can be considered as constant with time, the major magnetospheric currents systems are highly variable as a result of their control by the solar wind. The magnetopause currents for example typically cross the earth sunline approximately  $10 R_E$  up stream of the earth's center during quiet conditions (typically associated with a steady low speed solar wind). However, the magnetopause is on occasion observed to be inside geosynchronous orbit. During such periods the magnetic field is considerably distorted and the behavior of both naturally occurring and artificially injected charged particles is considerably different than during quiet conditions.

Both naturally occurring and artificially produced time variations in the magnetic field cause currents to flow in the earth's crust which tend to shield the interior of the earth from the magnetic variations. These telluric currents also distort the magnetic field above the earth's surface. They have been studied in considerable detail with relation to naturally occurring magnetic variations. The distortion of the local magnetic field produced by telluric currents should be included in any study of the time varying magnetic field produced by a low altitude nuclear burst. An accurate computation of the field at the location of the ground based magnetometers must include the effects of these telluric currents.

In addition to the problems this variability creates for the accurate description of the magnetic field, the time varying nature of magnetic field produces an induced electric field that can strongly influence the behavior of low energy charged particles. The subject of induced electric fields is discussed in the paragraphs below.

Low energy charged particles are influenced by electric fields in the magnetosphere. The magnetospheric electric field has many sources (Table 2-1 lists some of the sources and gives the approximate electric field strength). These include electrostatic fields produced by charge separation along field lines. This phenomenon appears to occur in the auroral region

and is the source of acceleration for the auroral primary particles. It also acts to accelerate heavy ions into geosynchronous orbit from the ionosphere. An electric field associated with the convection of low energy plasma in the magnetosphere that is produced by a "viscous interaction" between the solar wind and magnetospheric plasma has been widely discussed but is not well understood quantitatively.

Table 2-1  
ESTIMATES OF INDUCED ELECTRIC FIELDS

$$\nabla \times \vec{E} = - \frac{\partial \vec{B}}{\partial t} \rightarrow E \propto \frac{\Delta B}{\Delta t} \ell_S$$

Source	B (gamma)	t (hours)	$\ell_S$ ( $R_E$ )	E (volts/m)
Daily wobble of dipole plus image	30	24.0	10.0	0.0005
Field aligned currents	250	0.25	0.1	0.004
Tail field collapse	50	0.25	10.0	0.09
Sudden commencement magnetic storm	1500	0.25	10.0	2.5

Electric fields induced by time variations in the magnetospheric magnetic fields, however, have been quantitatively represented and are quite well understood. One of the key goals of this contract has been to understand the ways in which these naturally occurring induced electric fields influence gross motions and structuring in the plume of a nuclear burst during late times. The magnetospheric electric field generally can be characterized by its variability. During "quiet times" the magnitude of the fluctuations in the electric field are typically as large as the field itself from the DC field to frequencies of several hertz. During disturbed



conditions the total electric field strength can increase dramatically and the fluctuations are a smaller fraction of the total magnitude.

The various sources of this induction electric field and its strength are discussed elsewhere in this report. In this contract effort we have dealt almost exclusively with the electric field induced by the daily wobble of the earth's dipole axes. Although other naturally occurring induced fields are much larger in magnitude, this particular source was studied because it is always present and it is well understood.

### Section 3

#### ELECTROMAGNETIC FIELDS

Models of the quiet time magnetospheric magnetic and electric fields are described in this section; also described are the possible extensions of these models to include effects due to a disturbed magnetosphere.

The model of the earth's external magnetic field was developed under other contracts and are fully documented elsewhere (Olson and Pfitzer, 1977). A brief description of the magnetospheric magnetic field is provided here in order to illustrate an example of naturally occurring time dependence of the magnetic field which has associated with it an induced electric field which is described in subsequent sections. (The same techniques used to obtain this magnetic field were later modified to allow calculations of magnetic signatures of artificial plasma clouds in the magnetosphere.) These techniques are quite general and can be applied to other plasma-field problems such as the nuclear weapon, multiple burst considered elsewhere in this report.

#### 3.1 THE MAGNETIC FIELD MODEL

In order to quantitatively determine the magnetic field in near earth orbit, it is necessary to first obtain quantitative representations of the magnetospheric current systems. They include the magnetopause current system, formed by the interaction of the solar wind particles with the total magnetospheric magnetic field, the tail current system produced by particles flowing across the tail of the earth's magnetosphere and returning on its boundary, and the quiet time ring current system produced by the motion of charged particles moving within the magnetosphere. The magnetopause current is formed by particles which interact with the earth's magnetic field and then return immediately to the magnetosheath. These particles interact with the current system only for fractions of seconds as they are deflected by

the magnetospheric magnetic field. The particles which form the tail currents remain part of that current system for as long as several days as they make their journey across the tail. The quiet time ring current system is formed by particles trapped along magnetic field lines in the inner magnetosphere. These particles may contribute to the currents for as long as weeks or even months. Although the magnetopause currents flow only on a surface (on the magnetopause itself) both the tail current system and the ring current particles are distributed over a large region of space in the magnetosphere. Thus, the ring and tail currents are initially represented in the form of wire loops. In the inner magnetosphere there is a nest of three sets of wire loops used to represent the ring current. The tail currents flow almost linearly across the upper and lower boundaries of the plasmasheet in the distant tail while close to the earth they curve around such that they are in close proximity to the ring current loops. The return path of the tail currents was constructed to flow approximately on the boundary of the magnetopause with the shape similar to that used in the determination of the magnetopause currents. A three-dimensional view of these current systems is shown in Figure 3-1.

The procedure for determining the appropriate values of these currents was as follows. The general form of the currents as suggested by the observations were used to select the positions of "wires" and the strength of the current flowing through each of them. Integration over these currents then yielded values of the field from the distributed currents that were added to the magnetopause magnetic field (which had been previously determined) and the earth's main field and compared with observations. Differences in the observed and computed values of the field were noted and changes made in the positions and strengths of the currents in order to decrease the differences. The first check on the model is to compare it with the observed magnitude of the external field. Other tests of the accuracy of the model are given below.

The total magnetospheric magnetic field can then be found by integrating over these external currents and adding the field produced by the earth's main field. However, this is a very time consuming process. For

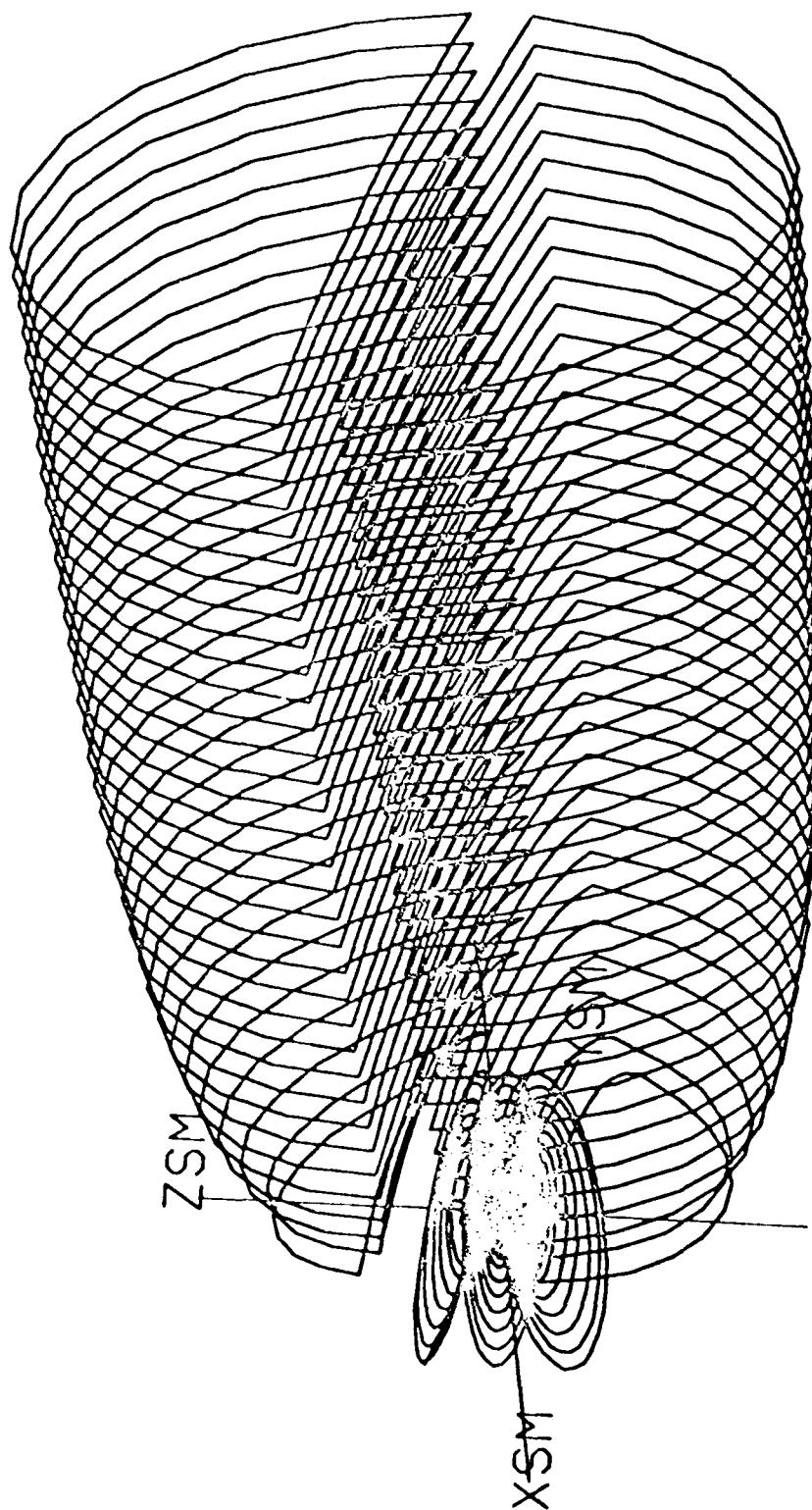
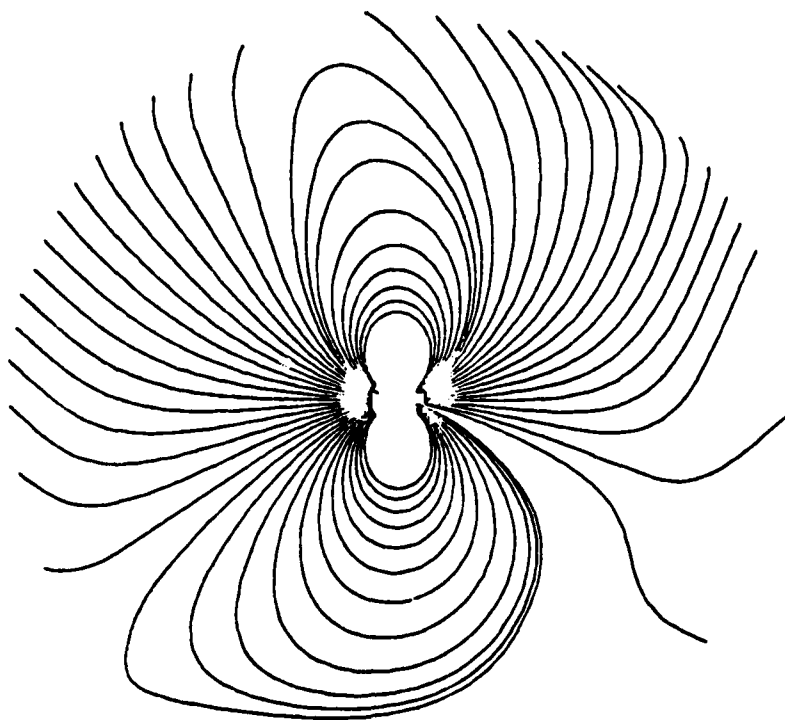


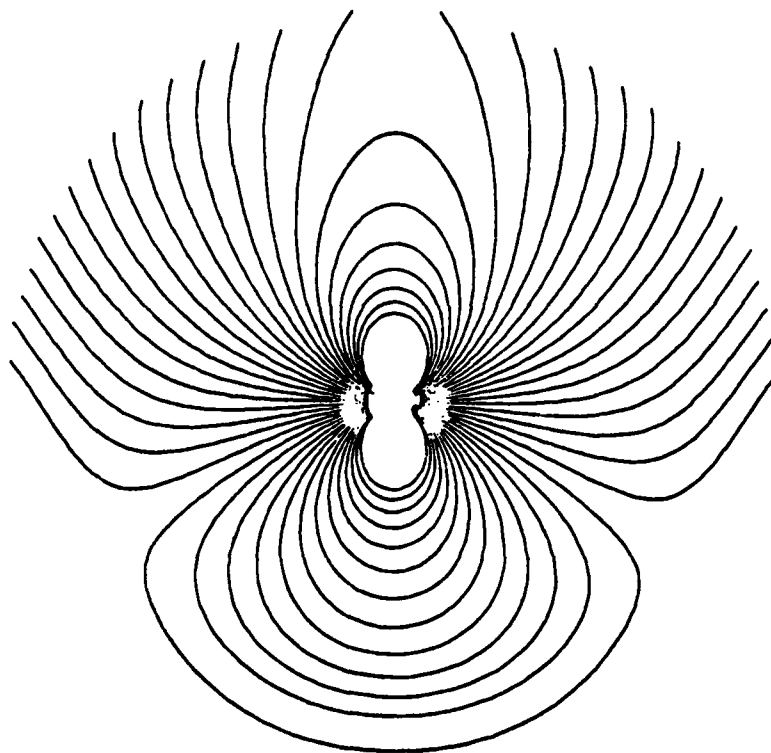
Figure 3-1. Three-dimensional View of the Current System for Tilt =  $0^\circ$

the model to be useful it must be capable of returning the total magnetospheric magnetic field at any position in the magnetosphere with a minimal expenditure of computer time. Therefore, the values of the magnetic field were found at many points by direct integration over the distributed and magnetopause currents. These values of the field were then input to a least squares best fit computer program to determine coefficients of the polynomial series to be used in the analytic field representation. Previous representations of the magnetopause magnetic field have been given in the terms of the scalar potential. Since the field from the distributed currents must be fit in the region of the source currents, a scalar potential can no longer be used since  $\nabla \times \bar{B}$  must be permitted to be nonzero. Another constraint on the form of the series representation is dictated by the rather sharp structuring that the field from the distributed currents exhibits in the inner magnetosphere. Thus, the series must simultaneously fit a very structured region near the earth and the weak field region in the distant tail. A standard one-dimensional orthogonal least squares fitting program was generalized for use to find coefficients in  $n$  variables. In order to fit both the structure of the inner magnetosphere and the tail field topology, it was necessary to include terms of up to sixth order in a power series plus similar terms multiplied by an exponential. A final requirement for the model is that the field must vary smoothly between the points where it was computed for input to the fitting program. Calculations of both the distributed magnetic field and the magnetopause magnetic field show that the model fields do vary smoothly over the region where they are defined. This finding is particularly important for the distributed magnetic field since "wires" were used initially to represent source currents. The form of the series representation for the distributed magnetic field and the coefficients have been published by Olson and Pfitzer (1974).

Field lines representing the total quiet time magnetospheric magnetic field are shown in the noon-midnight meridian plane for two angles of incidence of the solar wind on the dipole axis in Figure 3-2. It is this daily variation in tilt angle and the associated  $\partial \bar{B} / \partial t$  that induces an electric field throughout



TILT =  $-35^\circ$



TILT = 0

Figure 3-2. Field Lines in the Noon-Midnight Meridian Plane

the magnetosphere. The quantitative modeling of this electric field and induced electric fields in general is discussed in the next section. Note that the field line from  $76^\circ$  magnetic latitude cross the equator at midnight farther from the earth than the  $82^\circ$  lines in previous models. It is this feature, the extension of the near earth field lines produced by the inclusion of the distributed currents that makes this model capable of reproducing many particle and field observations that previously were not properly modeled.

The accuracy of the model has been tested by comparing model calculations with particle and field observations. Optical tracking data (Adamson, et al., 1973) from the NASA-MPE Barium Cloud Experiment has shown that the field lines in the inner magnetosphere are more elongated than the lines calculated from models consisting of main field and earlier external field representations (Barrish and Roederer, 1973). A computer program that combines any series expansion of the main field with various representations of the magnetospheric field used the IGS75 main field expansion and the present model to generate field lines and compare them with the optical track of the barium clouds (see Figure 3-3). The model field fits the observations quite accurately because it includes the depressed inner magnetosphere field feature produced by the quiet time ring current. The earth intercept of field lines from geosynchronous orbit have been determined for various local times (see Figure 3-4). The foot of the field line lies between  $65^\circ$  and  $66^\circ$  magnetic latitude depending on the time of day. This is almost  $3^\circ$  lower than the values given by previous boundary models.

### 3.2 THE ELECTRIC FIELD MODEL

Current understanding of the magnetospheric electric field is incomplete. Although data on this electric field are becoming increasing available, there is currently no quantitative description of the various sources of the magnetospheric electric field. The one source of these fields which is relatively well understood is the time variation in the magnetic field. A model of the quiet time tilt dependent magnetic field was examined in the preceding section, and its extension to include distributed magnetospheric effects is discussed in the following section (Section 3.3). These

42498A

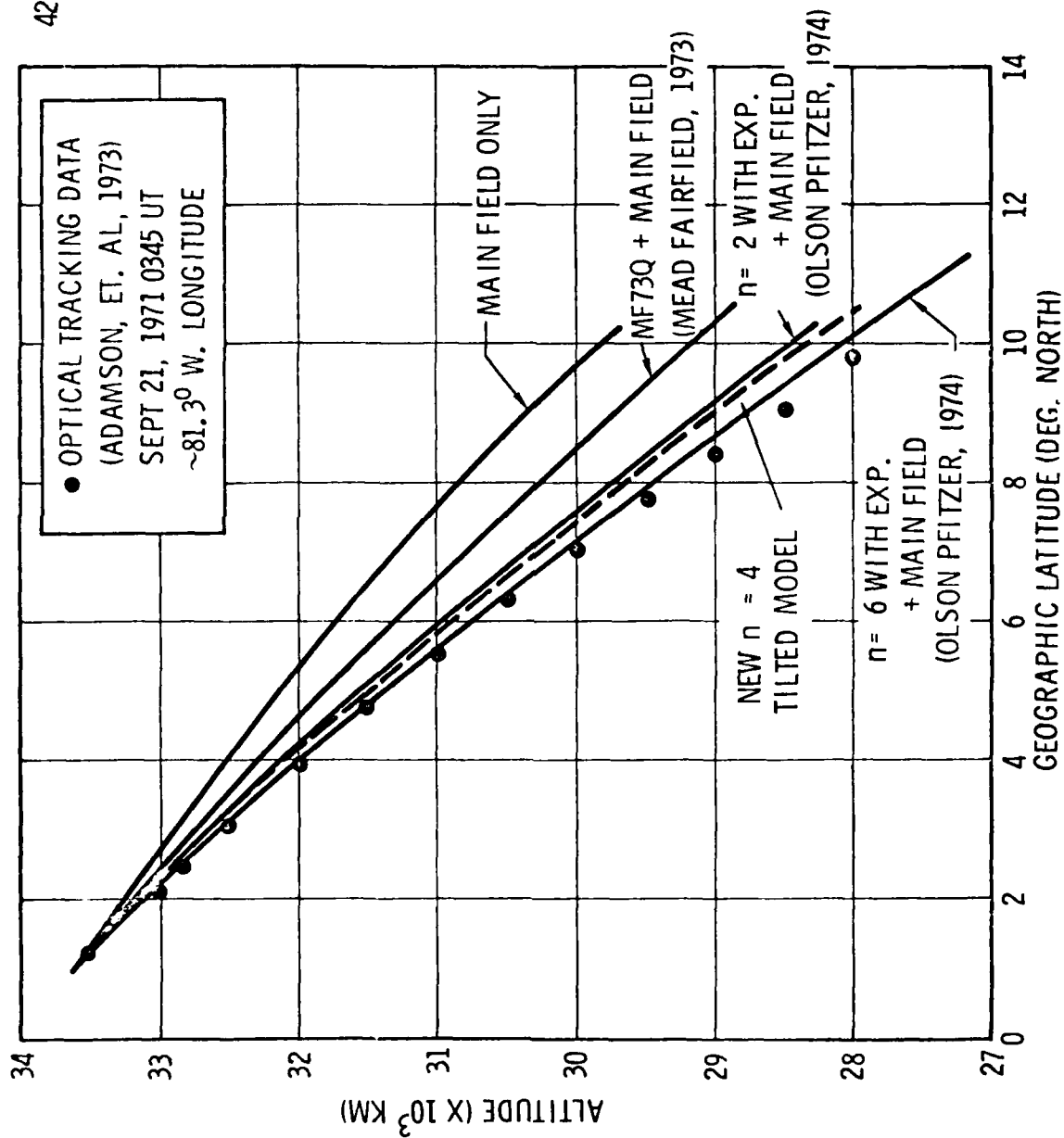


Figure 3-3. Optical Tracking Data of the Barium Clouds.



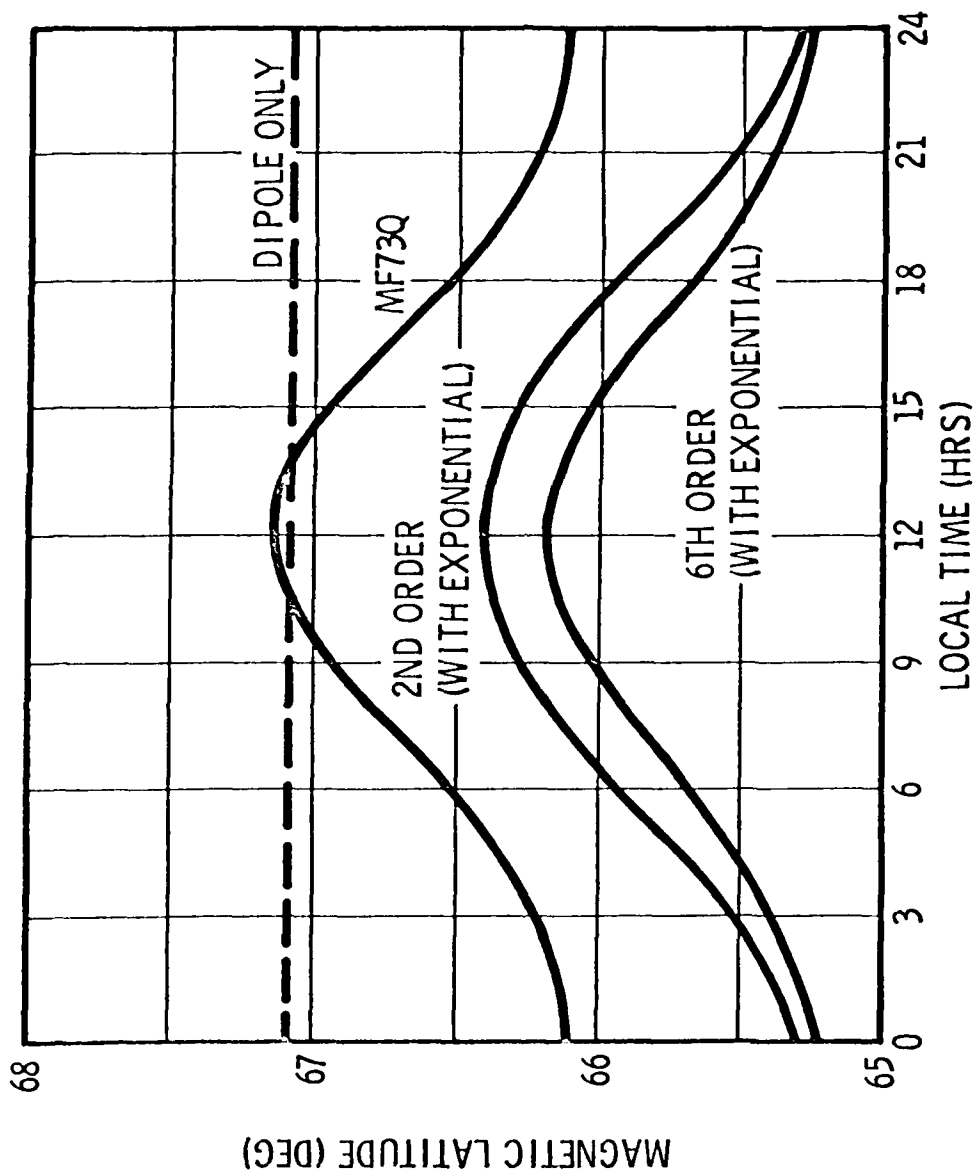


Figure 3-4. Earth Intercept of Field Lines for Geosynchronous Orbit.

models consider the time variations in all the major magnetospheric current systems as sources of the total external magnetic field.

The electric field model described in this section results from the diurnal fluctuations of the magnetic field model caused by the solar wind plasma - geomagnetic dipole field interaction. It is emphasized that the procedure used to obtain this electric field can equally well include any electric fields induced by temporal fluctuations in the magnetic field.

The procedure described in Section 3.1 described models of the magnetospheric current systems; the Biot-Savart law is applied to these currents to yield the magnetic field, thus

$$\vec{B}(\vec{r}) = \frac{\mu_0}{4\pi} \int \vec{J}(\vec{r}') \times \frac{(\vec{r}-\vec{r}')}{|\vec{r}-\vec{r}'|^3} dV'.$$

Because of the complexity of this current system, the integral is performed numerically. Similarly, and with very little additional cost in computer time, the vector potential for this field can also be obtained,

$$\vec{A}(\vec{r}) = \frac{\mu_0}{4\pi} \int \frac{\vec{J}(\vec{r}')}{|\vec{r}-\vec{r}'|} dV'.$$

Since the magnetospheric current system model includes a dependence on the daily precession of the earth's dipole moment, this particular time dependence of the magnetic field and the associated vector potential are properly modeled. The induced component of the magnetospheric electric field resulting from this dependence of the magnetic field can be obtained from the vector potential

$$\vec{E}_I = - \frac{\partial \vec{A}}{\partial t}.$$

Because of the presence of charged particles (low density plasma) throughout the magnetosphere (this medium is the source of the current system), local electric fields resulting from this medium must also be considered.

Indeed, the total electric field at a given location will not only include the contribution from the local time dependence of the magnetic field, but also contributions from other regions of the magnetosphere transmitted to this location by the medium, to the extent that it is conductive. Thus, the total electric field,

$$\vec{E}_T = - \nabla\phi - \frac{\partial \vec{A}}{\partial t} ,$$

at a given point in the magnetosphere includes contributions from the induced field from other regions of the magnetosphere, linked to the given location by the conductivity of the medium, as well as any contributions from location by the conductivity of the medium, as well as any contributions from local charge separation in the medium. This dependence is contained in the scalar potential component,  $\vec{E}_S = \nabla\phi$  of the total field.

A procedure developed by Hones and Bergeson (1965) was applied to evaluate the scalar potential component of the electric field. It is assumed that in the region of interest, charged particle densities are high enough to assure sufficient conductivities along the magnetic field lines such that  $\vec{E}_T \cdot \hat{B} = 0$ .

Then

$$\frac{d\phi}{ds} = \frac{\partial A_{||}}{\partial t} ,$$

where  $d\phi/ds$  is the scalar potential gradient along the field line, and  $\partial A_{||}/\partial t$  is the component of  $\vec{E}_T$  parallel to the magnetic field line. This equation can be integrated along the field line to give the scalar potential at a given point in the magnetosphere. Thus,

$$\phi(r) = \phi_B - \frac{\partial}{\partial t} \int_{FL} \bar{A} \cdot d\bar{s} ,$$

where the line integral is along the field line, and  $\phi_B$  is the potential at some appropriate boundary.

In the modeling of a realistic total electric field, care must be taken in the selection of the proper boundary condition as well as the value of  $\partial A_{||}/\partial t$  to be used in the integral. The presence of the medium complicates matters and careful estimates of the charged particle densities along the integration path must be made. If conductivities along the field line are sufficiently high, the induced electric field will propagate through very short distances and only local contributions of  $\bar{E}_I$  will be significant. At lower densities, the integral may be extended along the magnetic field lines but then the question of the appropriate boundary condition must be considered. The various options available for the selection of  $\partial A_{||}/\partial t$  are summarized in Table 3-1.

Table 3-1  
VALUE OF  $\frac{\partial A_{||}}{\partial t}$

1.  $\frac{\partial \bar{A}_{total}}{\partial t} = 0$  :  $\bar{E}_{total} = -\nabla\phi$  (time independent  $\bar{B}$ )
2.  $\frac{\partial \bar{A}_{||}}{\partial t} \neq 0$  : if  $\bar{E} \cdot \hat{B} = 0$ , then  $\frac{d\phi}{ds} = \frac{\partial A_{||}}{\partial t}$  (Hones and Bergeson; Ionized Media Assumed)
3.  $\frac{\partial A_{||}}{\partial t} \sim 0$  : by energy dissipation    A.  $d\phi/ds = \partial A_{||}/\partial t|_{local}$   
B.  $d\phi/ds \sim 0$  due to high conductivity
4.  $\frac{\partial A_{||}}{\partial t} \neq 0$  : if  $\bar{E} \cdot \bar{B} \neq 0$ , then  $d\phi/ds = ?$

The simple case of time independent  $\bar{B}$  is included here only for completeness, since it does not represent a very interesting case. It is consistent, however, with the assumption of magnetic field lines being equipotentials in an ionized medium. The second case represents the Hones and Bergeson procedure (discussed above) which is appropriate in regions where the conductivity along field lines is high enough so that  $\bar{E} \cdot \bar{B} = 0$ . The principal questions in applying this procedure is the selection of an appropriate boundary condition and the sources of magnetic field which contribute to  $\partial A_{||}/\partial t$ . In the limit of very high conductivities,  $\partial A_{||}/\partial t$  approaches zero through energy dissipation, and only local sources of the magnetic field contribute. Case 3 illustrates this condition; again the magnetic field lines will either approximate equipotentials or only local sources of  $\partial A_{||}/\partial t$  will contribute to  $\bar{E}$  parallel to the magnetic field line.

Case 4, in Table 3-1, represents the conditions present in areas where the conductivity along field lines is so low that  $\bar{E} \cdot \bar{B} \neq 0$ . The procedures discussed in this report are no longer appropriate for this case and the only available approach is the solution of the wave equation. This could be done if a particularly convenient boundary condition for the regions of interest could be postulated.

Options for the selection of the appropriate boundary condition for  $\phi$  include the following:

1. Experimentally determined.
2. Constant over an appropriate surface.
3. Uniformly magnetized rotating sphere (Hones and Bergeson, 1965),

$$V = \bar{U} \cdot \bar{A},$$

where  $V$  = the potential at point  $\bar{r}$ ,

$$\bar{U} = \bar{\omega} \times \bar{r},$$

$$\bar{A} = \bar{\mu} \times \bar{r}/R_S^3$$

$\bar{\omega}$  = angular velocity

$\bar{\mu}$  = magnetic moment

$R_S$  = radius of sphere.

4. A self-consistent rigorous determination of  $\phi$  and  $\bar{A}$ .

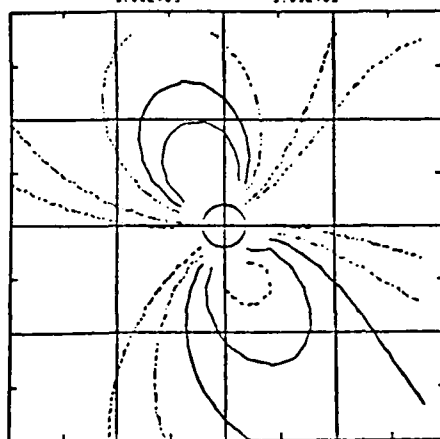
In the present work, options 2 and 3 were employed to evaluate the sensitivity of the electric field model to both the choice of the boundary condition and the nonlocal contributions to the induced electric field. Some results of this investigation are illustrated in Figures 3-5 and 3-6. In both figures, equipotential contours are plotted in the earth's equatorial plane. The positive x-direction in both plots is through the Greenwich meridian. The calculations were done in an inertial coordinate system in which the earth is rotating, the induced electric field (i.e.,  $\partial A_{\parallel}/\partial t$ ) is due to both the dipole field and the diurnal variations in the current systems. In both figures four calculation times are illustrated: thus, for example, in Figure 3-5a, the calculation time is UT (Universal Time) = 0.0 hours, summer solstice, when the Greenwich meridian (positive x-direction) is at midnight. In Figure 3-5b, the calculation is at UT = 6.0 hours when the Greenwich meridian is at dawn (i.e., the sun is in the positive y-direction). Similarly, Figures 3-5c and 3-5d are at UT = 12.0 and 18.0 hours when the Greenwich meridian is at noon (the sun is in the positive x-direction) and dusk (the sun is in the negative y-direction), respectively.

In Figures 3-5a through 3-5d, a uniform (constant) potential surface at  $R = 1 R_E$  was used as the boundary condition; while in Figures 3-6a through 3-6d rotating, uniformly magnetized sphere was used at the boundary of  $R = 1 R_E$ . The sensitivity to boundary conditions is clearly evident. The asymmetry in both sets of figures is due to the induced electric field resulting from time variation of the magnetospheric current system. This is particularly noticeable in Figures 3-6a through 3-6b where without the current system the contours would be circular.

In Figures 3-5a through 3-5d the change in potential,  $\phi$ , between the ionosphere (where it is assumed to be zero) and the equatorial plane is illustrated. Comparison of these Figures 3-5 and 3-6 suggests that if the ionospheric electric field (and  $\phi$ ) is variable, the total electric field in the magnetosphere will also vary substantially with time. Thus, through this mechanism, the ionosphere may exert some influence on the dynamics of magnetospheric fields and low energy plasma.

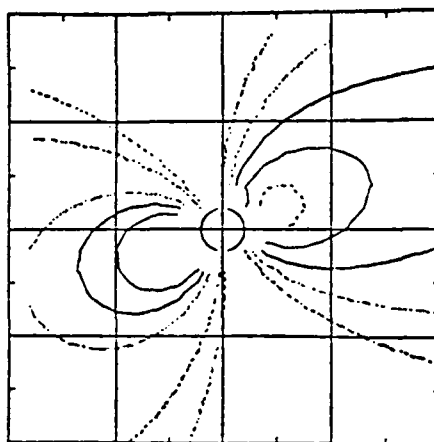
KEY TO CONTOURS

—	8.00E+03	—	-7.00E+03
—	7.00E+03	—	-6.00E+03
—	6.00E+03	—	-5.00E+03
—	5.00E+03	—	-4.00E+03
—	4.00E+03	—	-3.00E+03



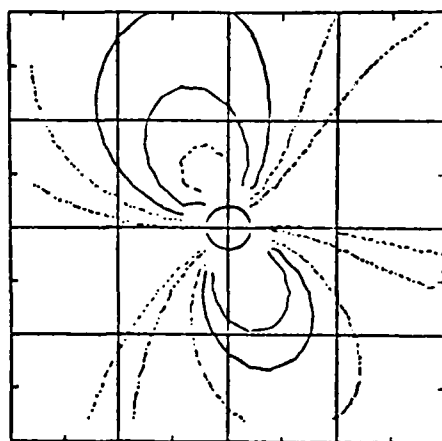
DAY= 172.00 UT = 0.00

(a)



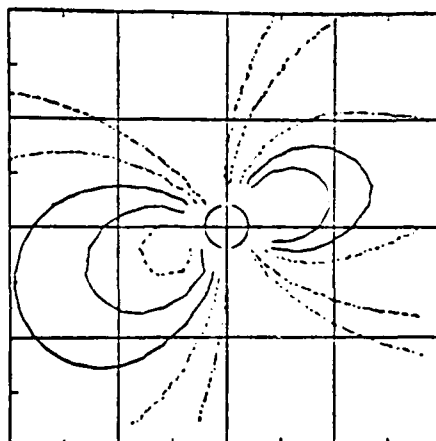
DAY= 172.00 UT = 6.00

(b)



DAY= 172.00 UT = 12.00

(c)



DAY= 172.00 UT = 18.00

(d)

Figure 3-5. Equipotential contours (in volts) in the equatorial plane, inertial frame, for a uniform boundary condition at  $r = 1 R_E$ . (The scale is  $5 R_E$  per major division.)

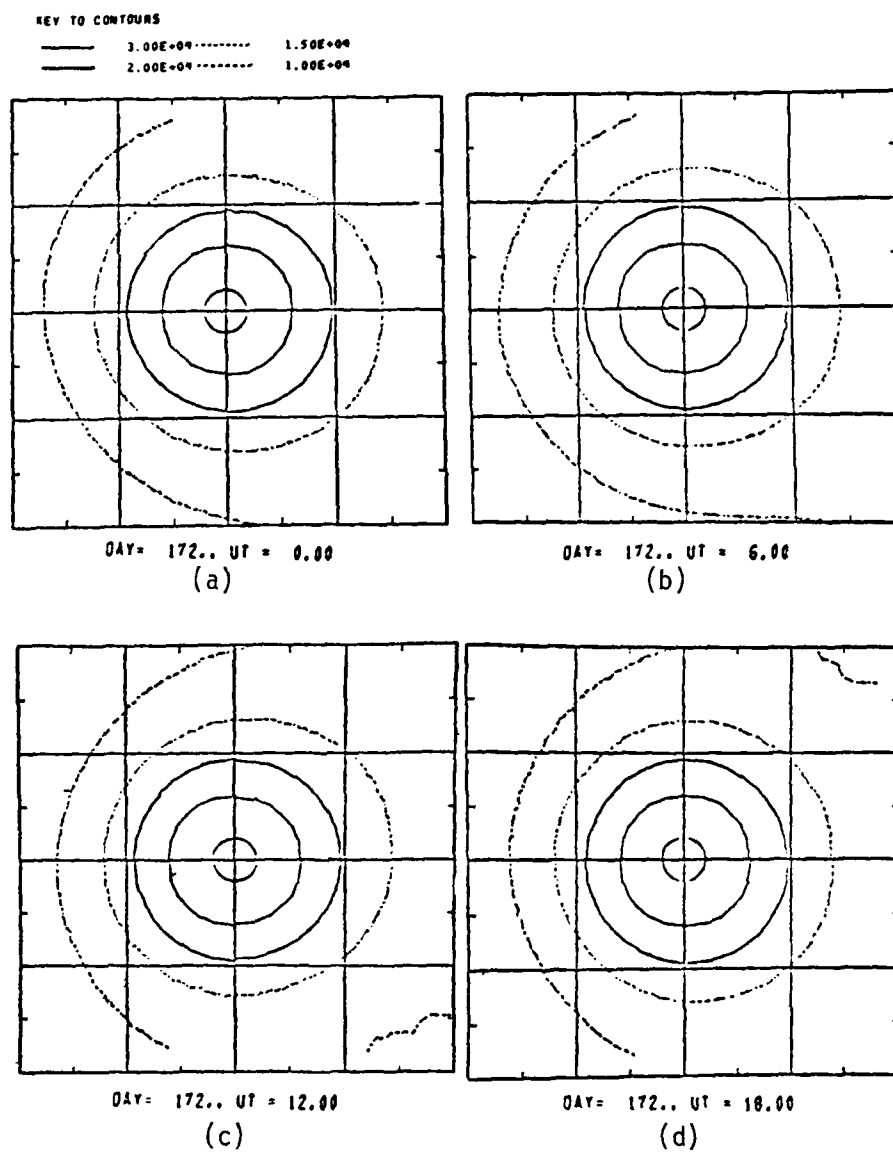


Figure 3-6. Equipotential contours (in volts) in the equatorial plane (inertial frame) for a rotating magnetized sphere boundary condition at  $r = 1 R_E$ . (The scale is  $5 R_E$  per major division.)



Also, Figure 3-5 indicates the change in  $\phi$  between the ionosphere and the equatorial plane when the ionospheric value of  $\phi$  is taken to be zero. Thus, magnetic field lines are not equipotentials even when only the "small" induced fields like the wobbling dipole are present.

The various components of the total electric field which would be "felt" by a charged particle rotating with the earth in geosynchronous orbit are illustrated in Figures 3-7 and 3-8. The uniformly magnetized, rotating sphere boundary condition was used for these calculations. Figure 3-7 displays the field as a function of longitude; Figure 3-8, the electric field as a function of time. Contours of constant  $|\bar{E}_{\text{total}}|$  in the equatorial plane are shown in Figures 3-9 and 3-10 for the rotating magnetized sphere boundary condition. Figures 3-9a through 3-9d are for the total electric field in an inertial frame at four times (UT = 0, 6, 12, and 18 hours, respectively). The contours, like those for the potentials (Figures 3-5 and 3-6), are plotted in geographic coordinates; all comments about the location of the axis with respect to the sun made above, are applicable here. Figures 3-10a through 3-10d are for the total field in the rotating coordinate system.

To indicate how a field such as the one illustrated in Figures 3-9 and 3-10 would contribute to charged particle acceleration, the time rate of change of a proton's kinetic energy was calculated using the formula from Northrop (1963)

$$\frac{d\langle w \rangle}{dt} = q \bar{E} \cdot \bar{V} + M \frac{\partial B}{\partial t} ,$$

where  $\langle w \rangle$  is the kinetic energy averaged over a gyration period,  $M$  is the magnetic moment of the proton,  $q$  its charge, and  $\bar{V}$  the velocity of its guiding center. The results of this calculation are shown in Figures 3-11 and 3-12. Figure 3-11 shows the energy gained by the guiding center of motion as a function of the guiding center kinetic energy, and similarly, Figure 3-12 shows the energy change in the motion about the guiding center.

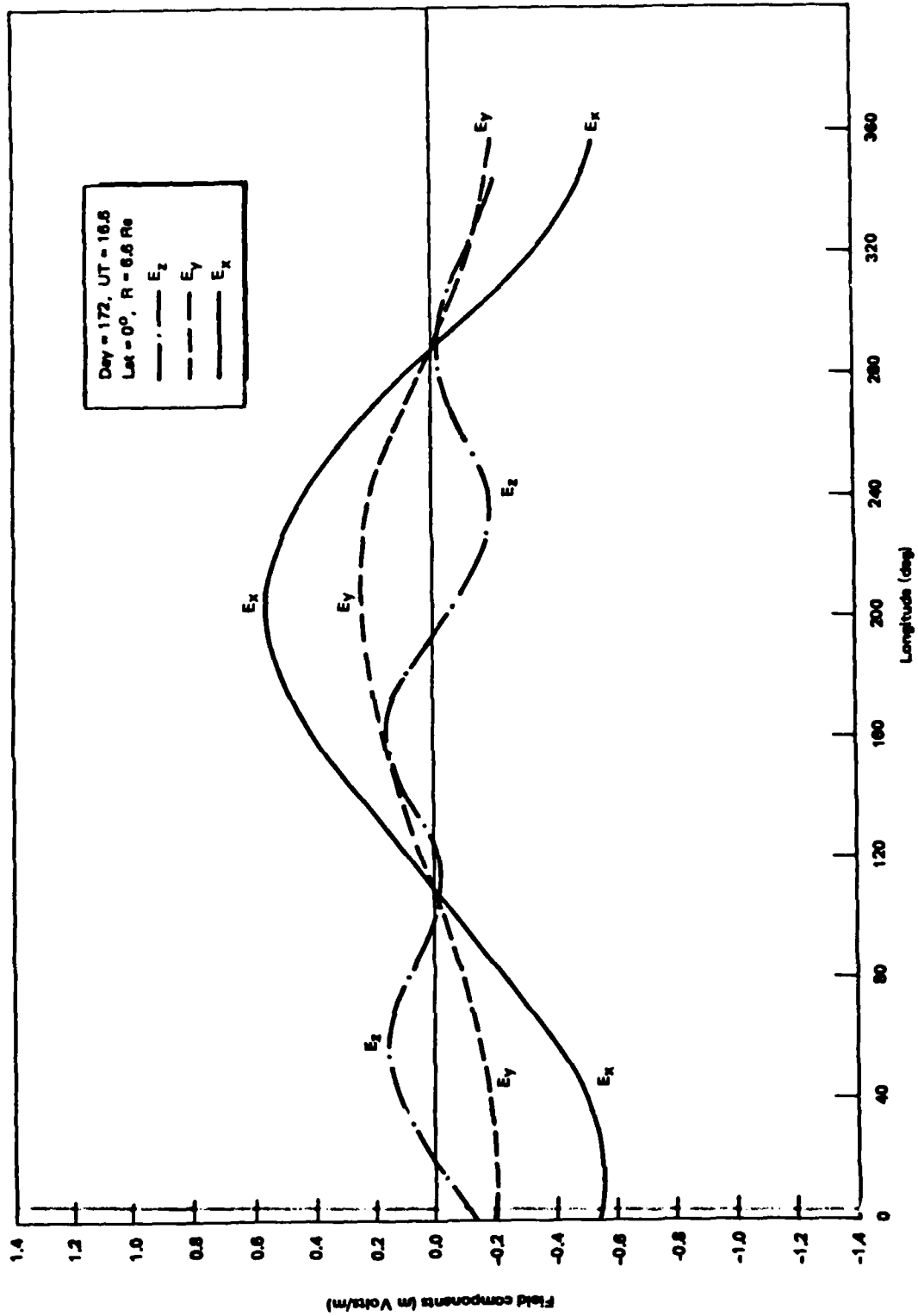


Figure 3-7. Total Electric Field Experienced by a Charged Particle Rotating with the Earth at Synchronous Orbit

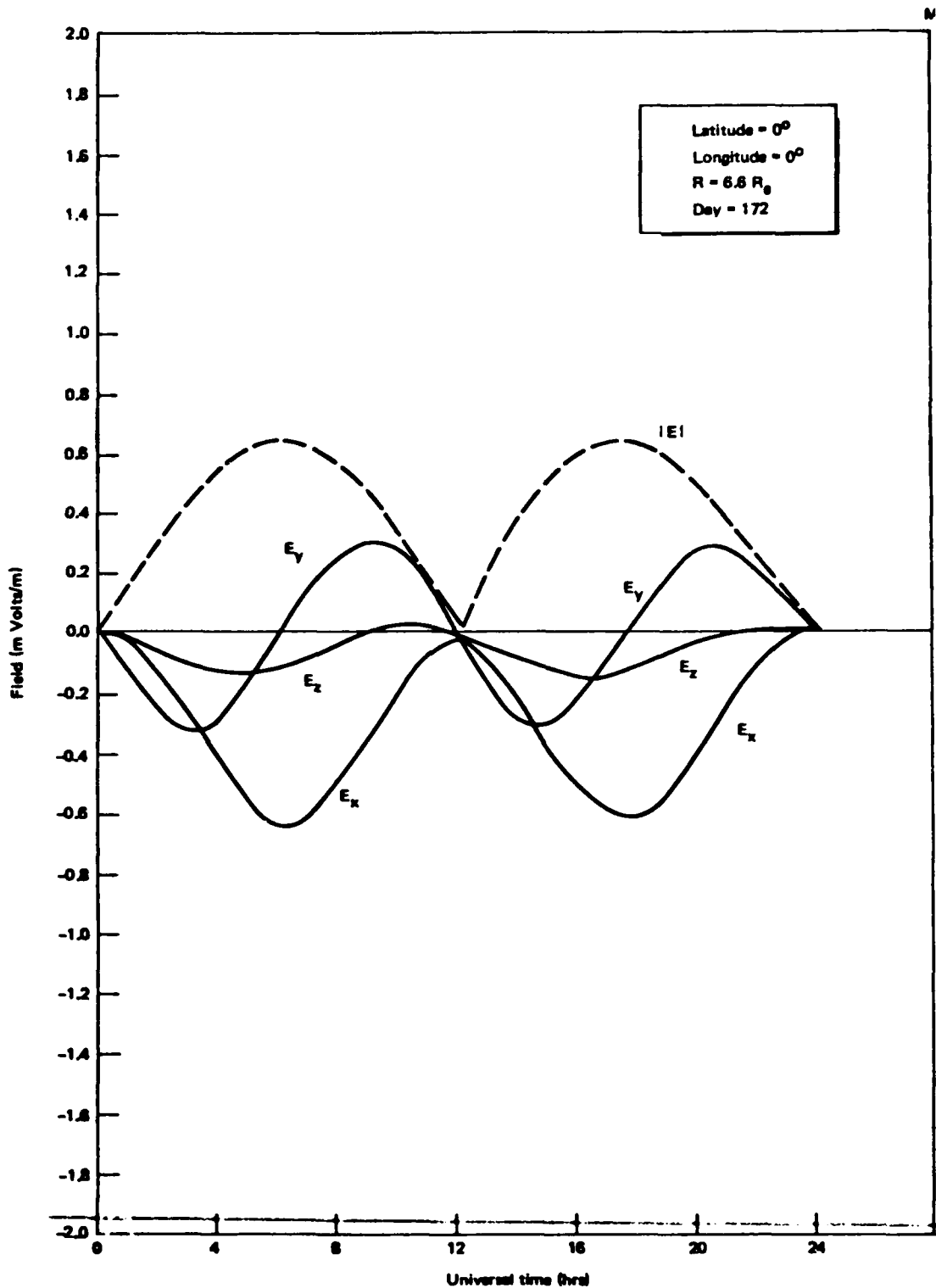


Figure 3-8. Total Electric Field Experienced by a Charged Particle Rotating with Earth at Synchronous Orbit

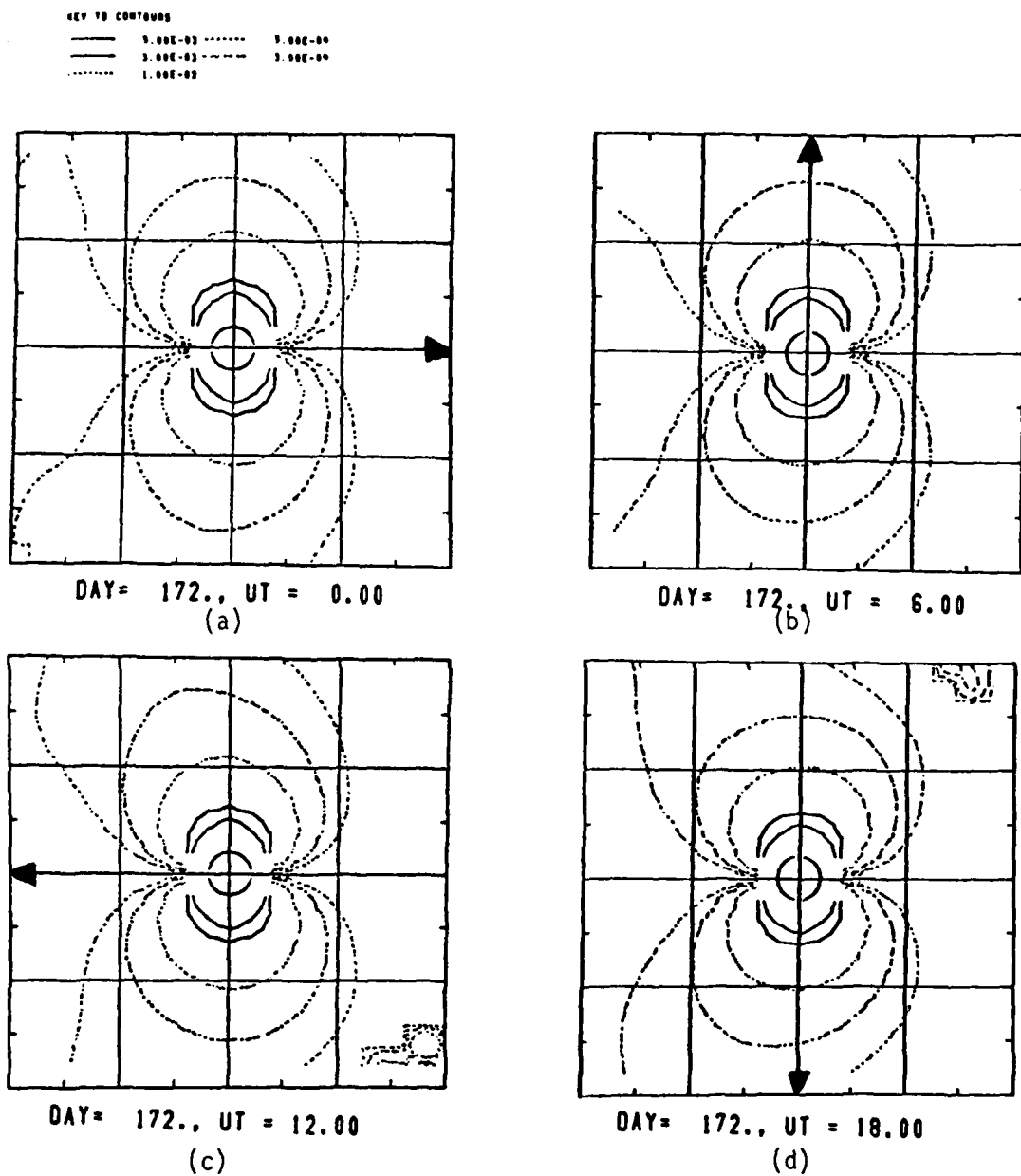


Figure 3-9.  $|E_{\text{total}}|$  in a rotating frame for a rotating uniformly magnetized sphere boundary condition. (Units are volts/meter and the major divisions are  $5 R_E$ .)

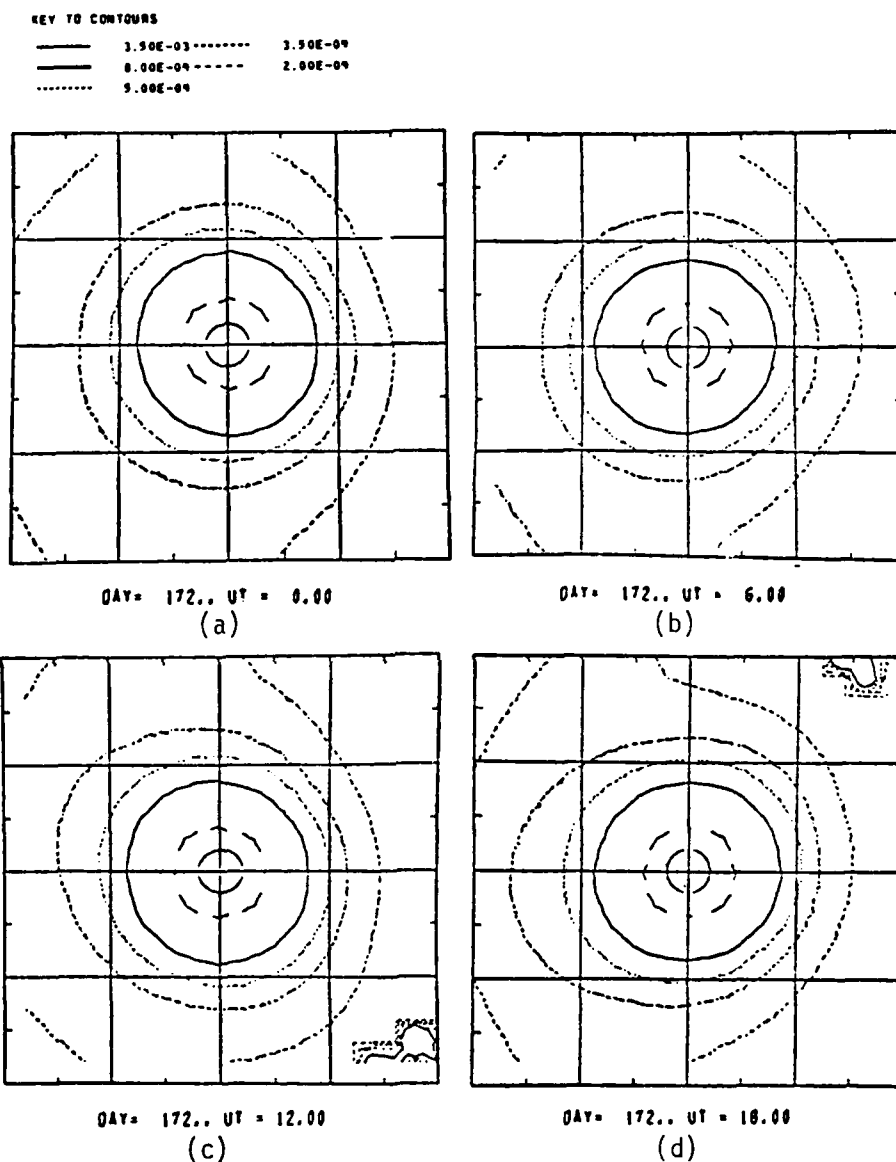


Figure 3-10.  $|E_{total}|$  in the inertial frame, rotating magnetized sphere boundary condition. (Units are volts/meter, the scale is  $5 R_E$  per major division.)

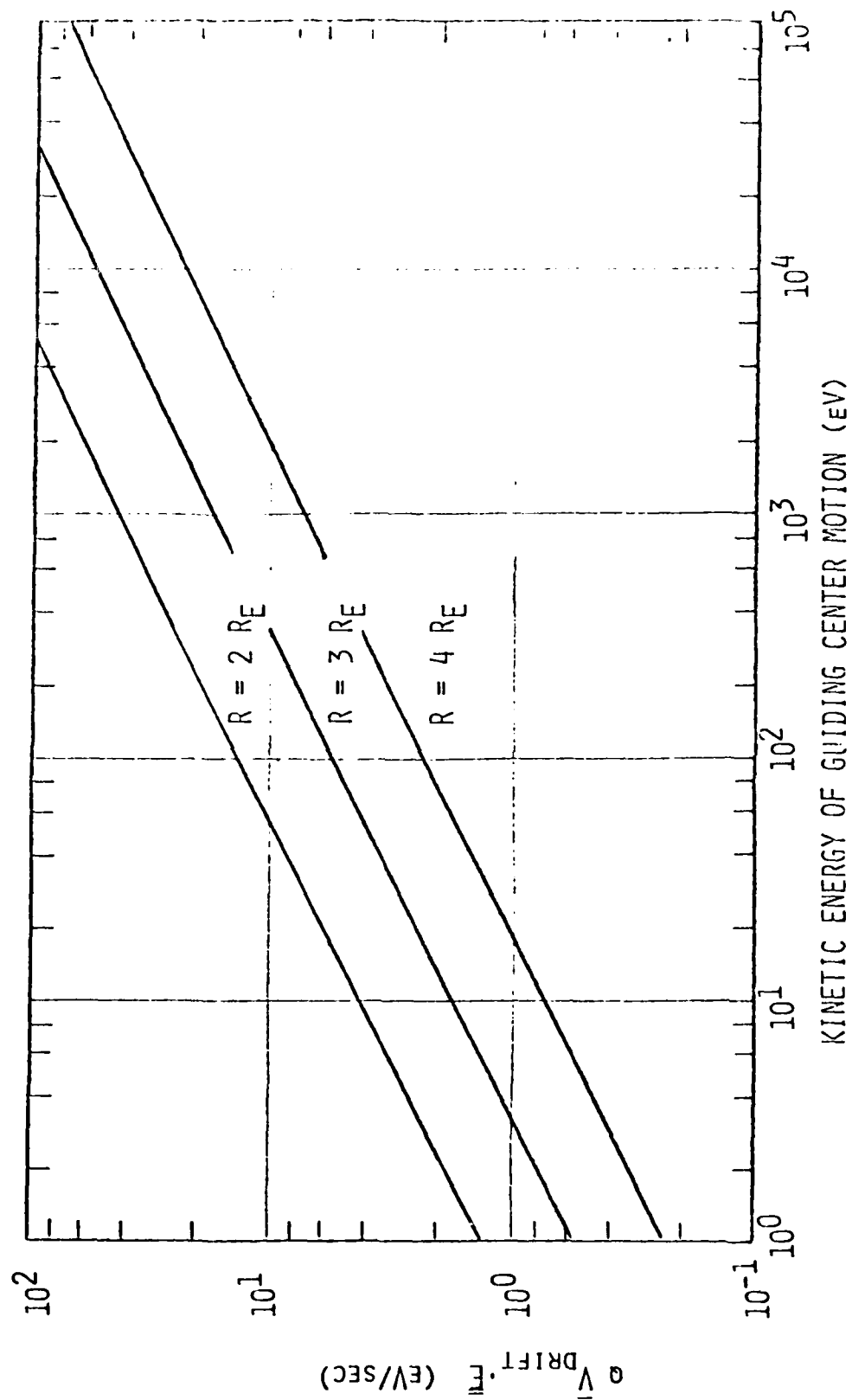


Figure 3-11. Time Rate of Change of Proton Kinetic Energy, Guiding Center Motion Contribution  
(UT = 16.6 Hrs., Day = 172, Equatorial Plane, Longitude = 0°).

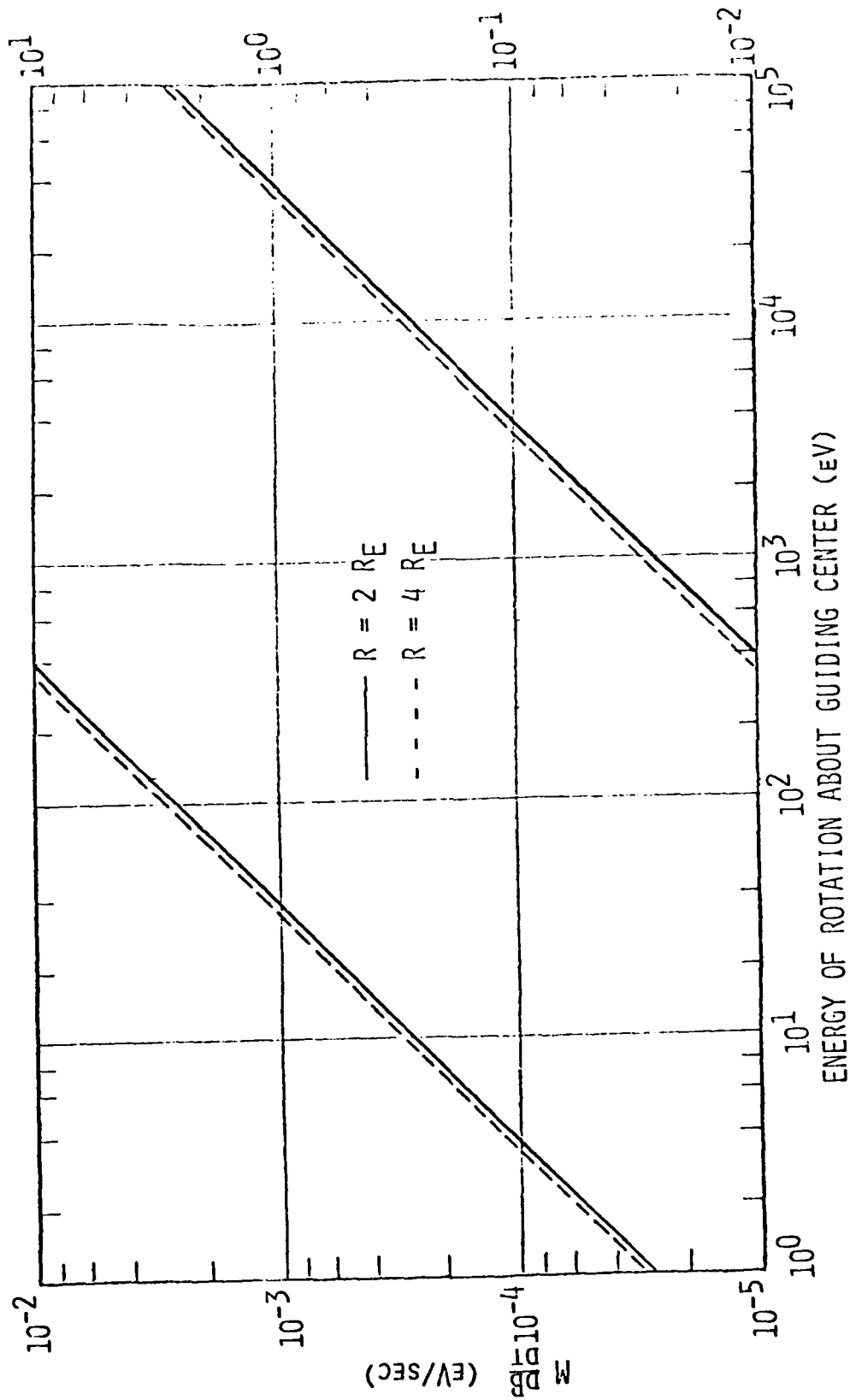


Figure 3-12. Time Rate of Change of Proton Kinetic Energy Due to Rotation About the Guiding Center  
(UT = 16.6, Day = 172, Equatorial Plane, Longitude = 0°).

### 3.3 EXTENSIONS OF THE MODELS

In the previous section the electric field from the time varying magnetic field resulting from the diurnally wobbling dipole was discussed. The procedures and methods used in that section are applicable to any electric field produced by a time varying magnetic field.

Recently (Olson, et al., 1979) a magnetic field model was developed that represents the earth's external magnetic field during disturbed times. In the new model the strengths of the three current systems can be varied separately. It is thus possible to describe the time varying magnetic field associated with dynamic processes in the magnetosphere such as magnetic storms and magnetospheric substorms. The magnetic vector potential is also determined and can be used to describe the induced electric field associated with time variations in the magnetic field. The electric fields associated with the storm time variations are considerably larger than the fields described in the previous sections.

For high latitudes the field line topology changes dramatically with small changes in the magnetospheric tail current systems. Figure 3-13 shows a field line originating at  $72^\circ$  magnetic latitude for varying strengths of the tail field (0.7 to 1.4 of normal in steps of 0.1). The equatorial crossing point varies from about  $13 R_E$  to over  $60 R_E$ .

The procedures developed for modeling the quiet time tilt dependent and the disturbed time magnetic and induced electric fields are directly applicable to the DNA efforts. The electric field from these time varying currents are found to be important for plume motions and plume structures in certain altitude and latitude regimes. Furthermore the computer codes developed to model the fields are directly usable for calculating the magnetic and self induction fields from a plume. Such a sample calculation is given in Section 5 for a sample 4 megaton burst.



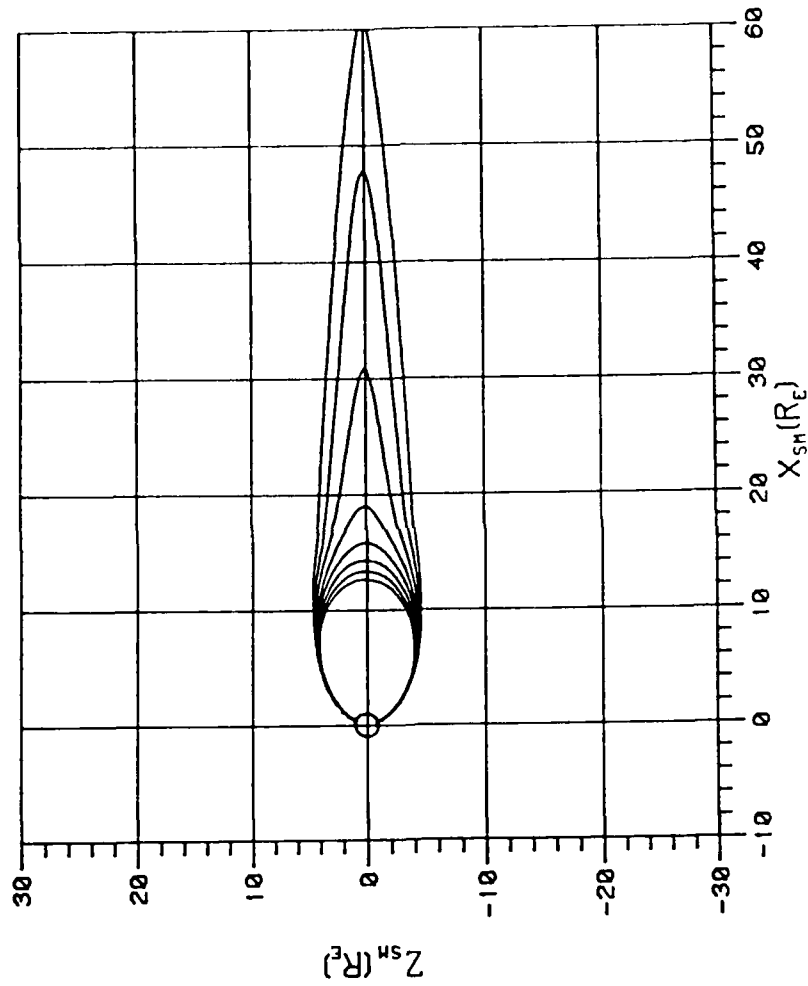


Figure 3-13. Field Line Originating at  $72^\circ$  Magnetic Latitude for Varying Strengths of the Tail Field.

Section 4  
INTERACTION OF  
ARTIFICIALLY PRODUCED PLASMA WITH NATURAL FIELDS

4.1 STRUCTURE AND MOTION OF ARTIFICIAL PLASMA IN THE NATURAL FIELD

4.1.1 Plasma Characteristics in a Low Frequency Field

Electric fields observed in the magnetosphere have been discussed in Section 2 and techniques which can be used to model these fields were discussed in Section 3.2. Interaction of these fields with artificially produced plasmas may influence the structure and motion of these plasmas even though the internal fields of the plasmas themselves may be larger than those external fields. The induced electric field which results from the diurnal variations in the magnetosphere has been examined quantitatively as an example. This field, although small in magnitude ( $\sim 0.1$  mVolt/m), is always present and because of its very low frequency may penetrate artificially injected plasmas in the ionosphere and magnetosphere.

The degree of penetration and internal magnitude of these fields depends on the detailed structure of the plasma. It is shown, however, that under conditions, which an artificially produced plasma at high altitudes is sure to attain, these natural electric fields can become important. The regime in question (called "electromagnetic" regime) is that state of the plasma in which the mean free path of the plasma particles and the plasma scale size are much greater than the particle Larmor radius.

All naturally occurring gross magnetospheric electric fields are slowly varying in time when compared to such quantities as the cyclotron and collision frequencies of the plasma particles. Because of this slow variation of the field, when considering the interaction of the background field and injected plasma, the plasma may be characterized by a dielectric constant and the degree of penetration of the field by the skin depth. The resulting

electromagnetic field equations, plasma conductivities and dielectric constants are discussed in Appendix A.

To simplify the problem, certain convenient approximations were employed; the general procedure is that followed in Frances and Perkins (1975).

Langevin's equations, which are adequate approximations for the cold and/or long wavelength plasma regime of interest here, are used to represent the motions of the electrons (subscript e) and the positive ions (subscript i),

$$m_e \frac{d\bar{V}_e}{dt} + m_e \nu_{en} \bar{V}_e + m_e \nu_{ei} (\bar{V}_e - \bar{V}_i) = -e(\bar{E} + \bar{V}_e \times \bar{B})$$

and

$$M_i \frac{d\bar{V}_i}{dt} + M_i \nu_{in} \bar{V}_i + M_i \nu_{ie} (\bar{V}_i - \bar{V}_e) = e(\bar{E} + \bar{V}_i \times \bar{B})$$

The neutrals are assumed to be at rest in the coordinate system used. To obtain the conductivities from these equations, one uses Ohm's Law

$$\bar{J} = \bar{\sigma} \cdot \bar{E}$$

and 
$$\bar{J} = N(e\bar{V}_i - e\bar{V}_e)$$

where  $N \approx N_e \approx N_i$ , the number densities of the ions and electrons.

To further simplify these equations, it is assumed that

$$\frac{d}{dt} = \frac{\partial}{\partial t} + \vec{V} \cdot \nabla \approx \frac{\partial}{\partial t}$$

and that the time dependence is  $e^{-i\omega t}$  (i.e., consider the electric field in terms of its Fourier components), where  $\omega$  is of the order of  $2\pi/(3600 \times 24) \sim 7.3 \times 10^{-5} \text{ sec}^{-1}$ . Thus, the real component of the Pedersen conductivity is given by

$$\begin{aligned} (\sigma_{xx})_r = (\sigma_{yy})_r = & \frac{n_e e^2}{m_e} \frac{(v_{en} + v_{ei})}{(v_{en} + v_{ei})^2 + (\omega_{ce}^2)} \\ & - \frac{n_i e^2 v_{ie}}{m_e} \left[ \frac{(v_{in} + v_{ie})(v_{en} + v_{ei}) + \omega_{ci} \omega_{ce}}{[(v_{en} + v_{ei})^2 + \omega_{ce}^2][(v_{in} + v_{ie})^2 + \omega_{ci}^2]} \right] \\ & + \frac{n_i e^2}{m_i} \frac{(v_{in} + v_{ie})}{(v_{in} + v_{ie})^2 + \omega_{ci}^2} \\ & - \frac{n_e e^2 v_{ei}}{m_i} \left[ \frac{(v_{in} + v_{ie})(v_{en} + v_{ei}) + \omega_{ci} \omega_{ce}}{[(v_{en} + v_{ei})^2 + \omega_{ce}^2][(v_{in} + v_{ie})^2 + \omega_{ci}^2]} \right] ; \end{aligned}$$

And, similarly, the Hall components of the conductivity are given by

$$(\sigma_{xy})_r = -(\sigma_{yx})_r = \frac{n_e e^2}{m_e} \frac{\omega_{ce}}{(v_{en} + v_{ei})^2 + \omega_{ce}^2}$$

$$\begin{aligned}
& - \frac{n_i e^2 \nu_{ie}}{m_e} \left[ \frac{\omega_{ce}(\nu_{in} + \nu_{ie}) - (\nu_{en} + \nu_{ei}) \omega_{ci}}{[(\nu_{ei} + \nu_{en})^2 + \omega_{ce}^2][(\nu_{in} + \nu_{ie})^2 + \omega_{ci}^2]} \right] \\
& - \frac{n_i e^2}{m_i} \frac{\omega_{ci}}{(\nu_{in} + \nu_{ie})^2 + \omega_{ci}^2} \\
& + \frac{n_e e^2 \nu_{ei}}{m_i} \left[ \frac{\omega_{ci}(\nu_{en} + \nu_{ei}) - \omega_{ce}(\nu_{in} + \nu_{ie})}{[(\nu_{ei} + \nu_{en})^2 + \omega_{ce}^2][(\nu_{in} + \nu_{ie})^2 + \omega_{ci}^2]} \right]
\end{aligned}$$

where  $\omega_{ce} = \frac{eB}{m_e}$  and  $\omega_{ci} = \frac{eB}{M_i}$ .

The component of the conductivity along the magnetic field line is

$$\begin{aligned}
\sigma_{zz} &= \frac{n_e e^2}{m_e(\nu_{en} + \nu_{ei})} - \frac{n_i e^2 \nu_{ie}}{m_e(\nu_{en} + \nu_{ei})(\nu_{in} + \nu_{ie})} \\
&+ \frac{n_i e^2}{m_i(\nu_{in} + \nu_{ie})} - \frac{n_e e^2 \nu_{ei}}{m_i(\nu_{en} + \nu_{ei})(\nu_{in} + \nu_{ie})}
\end{aligned}$$

where use was made of the fact that  $\omega$  is much less than the other quantities given above.

The collision frequencies appropriate for use in these equations are  
 $\nu_{en}$  = collision frequency of electrons with the neutrals

$$= 2.6(10^4) R^2 N_n T_e^{1/2}$$

and  $R$  = classical ion radius ( $\sim 10^{-10}$  m).

For the collision frequency of ions with neutrals, we use

$$\nu_{in} = \frac{6.1(10^2)\sigma^2}{\sqrt{W}} N_n T_i^{1/2} \quad , \quad \text{where } W \text{ is molecular weight of ions.}$$

The collision frequency of electrons due to ions

$$\nu_{ei} \approx 3.6(10^{-6}) N_i T_e^{-3/2} \log_e \left( \frac{1.23(10^7) T_e^{3/2}}{N_e^{1/2}} \right)$$

The collision frequency of ions with electrons

$$\nu_{ie} \approx \frac{m_e}{m_i} \nu_{ei} \quad .$$

In what follows, four regimes are considered:

1. The low altitude ( $B = 0.5 \times 10^{-5}$  Tesla) low density plasma ( $N = 10^{12} \text{ m}^{-3}$ ),
2. The low altitude, high density plasma ( $N = 10^{14} \text{ m}^{-3}$ ),
3. The high altitude ( $B = 1.0 \times 10^{-6}$  Tesla) low density plasma (again  $N = 10^{12} \text{ m}^{-3}$ ), and
4. The high altitude, high density ( $N = 10^{14} \text{ m}^{-3}$ ) plasma.

Further, the electron temperature is taken to be 1/2 eV or 5500°K and the neutral density in the low altitude regime is set at  $N_n \sim 10^{18} \text{ m}^{-3}$  and  $N_n \sim 0$  in the high altitude regime. The dominant species at both altitudes is assumed to be atomic oxygen. The resulting values of the relevant quantities in the four regimes are given in Table 4-1.

Table 4-1

	LOW ALTITUDE		HIGH ALTITUDE	
	$B=5 \times 10^{-6}$ Tesla	$N_N=10^{18} \text{ m}^{-3}$	$B=1.1 \times 10^{-6}$ Tesla	$N_N=0.0$
	Low Density $N_e=N_i=10^{12} \text{ m}^{-3}$	High Density $N_e=N_i=10^{14} \text{ m}^{-3}$	Low Density $N_e=N_i=10^{12} \text{ m}^{-3}$	High Density $N_e=N_i=10^{12} \text{ m}^{-3}$
$v_{en}$	$2 \times 10^4 \text{ sec}^{-1}$	$2 \times 10^4 \text{ sec}^{-1}$	0.0	0.0
$v_{in}$	$1.1 \times 10^2 \text{ sec}^{-1}$	$1.1 \times 10^2 \text{ sec}^{-1}$	0.0	0.0
$v_{ei}$	$1.4 \times 10^2 \text{ sec}^{-1}$	$1.0 \times 10^4 \text{ sec}^{-1}$	$1.4 \times 10^4 \text{ sec}^{-1}$	$1.0 \times 10^4 \text{ sec}^{-1}$
$v_{ie}:H^+$	$7.6 \times 10^{-2} \text{ sec}^{-1}$	5.44 sec <sup>-1</sup>	$7.6 \times 10^{-3} \text{ sec}^{-1}$	5.44 sec <sup>-1</sup>
$v_{ie}:O^+$	$4.7 \times 10^{-3} \text{ sec}^{-1}$	0.337 sec <sup>-1</sup>	$4.7 \times 10^{-3} \text{ sec}^{-1}$	0.337 sec <sup>-1</sup>
$\omega_{ce}$	$9 \times 10^5 \text{ sec}^{-1}$	$9 \times 10^5 \text{ sec}^{-1}$	$2 \times 10^5 \text{ sec}^{-1}$	$2 \times 10^5 \text{ sec}^{-1}$
$\omega_{ci}:H^+$	$4.9 \times 10^3 \text{ sec}^{-1}$	$4.9 \times 10^3 \text{ sec}^{-1}$	$1.1 \times 10^2 \text{ sec}^{-1}$	$1.1 \times 10^2 \text{ sec}^{-1}$
$\omega_{ci}:O^+$	$3 \times 10^2 \text{ sec}^{-1}$	$3 \times 10^2 \text{ sec}^{-1}$	6.74 sec <sup>-1</sup>	6.74 sec <sup>-1</sup>
Pederson:				
$R_e(\sigma_{xx})$	$\sim 1.7 \times 10^{-3} \text{ mho/m}$	$\sim 0.202 \text{ mho/m}$	$\sim 1.0 \times 10^{-6} \text{ mho/m}$	$\sim 8 \times 10^{-5} \text{ mho/m}$
Hall:				
$R_e(\sigma_{xy})$	$\sim 2.8 \times 10^{-4} \text{ mho/m}$	$\sim 2.8 \times 10^{-2} \text{ mho/m}$	$\sim 1.4 \times 10^{-3} \text{ mho/m}$	$\sim 0.15 \text{ mho/m}$
Parallel:				
$R_e(\sigma_{zz})$	$\sim 1.4 \text{ mho/m}$	$\sim 94 \text{ mho/m}$	$\sim 200 \text{ mho/m}$	$\sim 288 \text{ mho/m}$
Skin Depth Perpendicular:				
$\delta_L$	$\sim 2503 \text{ km}$	$\sim 232 \text{ km}$	$\sim 10^5 \text{ km}$	$\sim 1.2(10^4) \text{ km}$
Skin Depth Parallel:				
$\delta_{  }$	$\sim 88 \text{ km}$	$\sim 10.7 \text{ km}$	$\sim 7.5 \text{ km}$	$\sim 6.3 \text{ km}$

The most important parameter for considerations of field penetration into the plasma is the "skin depth" which is mathematically defined in Appendix A. It is that distance over which an oscillating electric field loses a factor of  $e$  of its energy. As can be seen, the electric field is expected to penetrate well into the plasma especially in the high altitude regime.

The strikingly large skin depths apply only to electromagnetic waves of the low frequencies ( $7.3 \times 10^{-5} \text{ sec}^{-1}$ ) considered here. For frequencies of the order of the cyclotron frequencies the character of the whole problem changes. For substorms which have typical frequencies a factor of a hundred larger than those above, the skin depths are only a factor of ten lower than those in the table. These skin depths are also large and similar conclusions about plasma penetration and structure can be made about those fields.

#### 4.1.2 Plasma Behavior in a Low Frequency Field

From simple arguments concerning conditions at the boundary of a plasma, it is clear that the component of the total electric field,  $\bar{E}$ , tangent to the boundary is continuous across the boundary and that the component of the electric displacement,  $\bar{D}$ , perpendicular to the boundary is also continuous across it. From such arguments it can be shown that a portion of the total field penetrates the plasma in an anisotropic manner causing distortion of the region. In the "equatorial region" of the plasma this penetration becomes important because the resulting  $\bar{E} \times \bar{B}$  drift are significant (relative to the magnitude and direction of the pressure gradient drift). (Equatorial regions are those regions of the farthest extent of a given magnetic field line in the vicinity of the magnetic equator.) The  $\bar{E} \times \bar{B}$  drift produces translation of the plasma and may also cause it to structure. At low altitudes the consequences of the anisotropic penetration of the electric field into the plasma is probably not significant because of the small value of the  $\bar{E} \times \bar{B} / B^2$  drift velocities there. However, the significant drift velocities that occur for the plasma in the equatorial region can appreciably translate the locus of the plume during late times.



Regions of sharp gradients (of plasma density) of a finite, inhomogeneous plasma can be approximated by a surface. Using Equation A-2 (see Appendix A) and Stoke's theorem gives

$$\oint_C \vec{E} \cdot d\vec{r} = \int_S (\nabla \times \vec{E}) \cdot \vec{n} da$$

$$= -i\omega \oint_S \vec{B} \cdot \vec{n} da$$

Since  $\vec{B} \cdot \vec{n}$  is continuous across the surface, so is the tangential component of  $\vec{E}$ . Using Equation A-3 and Gauss's law

$$\oint_S \vec{D} \cdot \vec{n} da = \int_V \nabla \cdot \vec{D} dv$$

gives

$$\vec{E} \cdot \vec{n} \Big|_{\text{inside plasma}} \approx \frac{\epsilon_{\text{plasma}}}{\epsilon_0} \vec{E} \cdot \vec{n} \Big|_{\text{outside plasma}}$$

$$\approx \frac{1}{\left| 1 + \chi_r - \frac{i\sigma_r}{\omega t_0} \right|} \vec{E} \cdot \vec{n} \Big|_{\text{outside plasma}}$$

If the plasma is sufficiently dense, the normal component of  $\vec{E}$  inside the plasma is much less than the normal component outside the plasma. The tangential component, however, does penetrate the plasma (see Appendix A for skin depth estimates) and for this component, geometrical considerations become important (see Figure 4-1). Due to geometric considerations alone, the tangential component of  $\vec{E}$  will be a maximum in regions where the surface normal becomes perpendicular to  $\vec{E}$  and a minimum when it becomes parallel to  $\vec{E}$ . If the skin depth ( $\sim 1/\sqrt{\omega\mu_0\sigma}$ ) is large, there will only be slight attenuation of this component in passing through the plasma.

In those regions where the tangential component of the  $\vec{E}$  field penetrates the plasma appreciable distances, the drift velocity of the plasma due to this field may become significant. The equations of motion of the plasma become

$$\frac{\partial(n_e V_e)}{\partial t} + \nabla \left( \frac{KT_e n_e}{m_e} \right) - \frac{e}{m_e} (E + V_e \times B) n_e = v_{ei}(V_e - V_i) n_e + v_{en}(V_e) n_e$$

$$\frac{\partial(n_i V_i)}{\partial t} + \nabla \left( \frac{KT_i n_i}{M_i} \right) + \frac{e}{M_i} (E + V_i \times B) n_e = v_{ie}(V_i - V_e) n_e + v_{in} V_i n_e$$

where all symbols are defined in Appendix B.

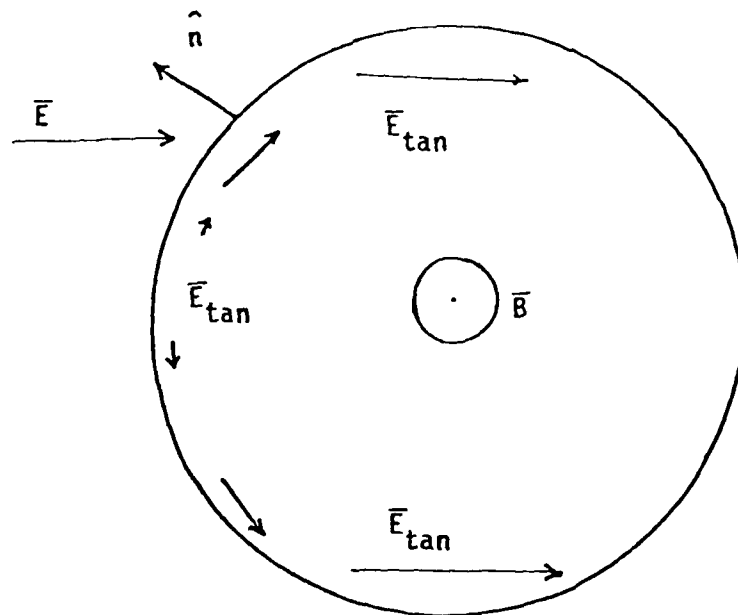


Figure 4-1. Geometrical Dependence of Penetrating Tangential Component of  $\vec{E}$

In Appendix B these equations are solved by making the following assumptions:

$$\frac{\partial(n\bar{V})}{\partial t} \sim 0 \quad , \text{ reasonable for slowly varying fields,}$$

$$v_{in}, v_{en} \quad , \text{ are negligible in the equatorial region of the plume}$$

$$\bar{V}_e \approx \bar{V}_i \quad , \text{ reasonable for small charge displacement,}$$

$$n_e \approx n_i \quad , \text{ quasi neutrality}$$

$$\text{and } T_e \approx T_i \quad , \text{ near ambient conditions.}$$

Under these conditions the solution for the component of  $\bar{V}$  perpendicular to  $\bar{B}$  is

$$\bar{V}_\perp = \frac{kT_e \nabla n \times \bar{B}}{qB^2} + \frac{\bar{E} \times \bar{B}}{B^2}$$

where  $q$  is the charge of the particle ( $\pm e$ ).

The second term on the right ( $\bar{E} \times \bar{B}$  drift) is independent of the particle charge and is the same for all species. On the other hand, the first term on the right (the density gradient motion) does depend on particle charge and is in opposite directions for ions and electrons. Also, since  $\nabla n$  is radial,  $\nabla n \times \bar{B}$  is azimuthal and does not contribute to translational motions of the plasma. The penetrating component of  $\bar{E}$  is also azimuthal (see Figure 4-1) hence  $\bar{E} \times \bar{B}/B^2$  is radial. The two types of drifts ( $\bar{E} \times \bar{B}$  and gradient) are not in the same direction. Thus, even for "small"  $\bar{E}$  fields, the  $\bar{E} \times \bar{B}$  drift causes significant displacement of the plasma over long times. This drift is summarized below for  $\bar{B}$  and  $\bar{E}$  values of interest.

#### ESTIMATES OF $\bar{E} \times \bar{B}/B^2$ DRIFT VELOCITY

	Observed Quiet Time $\bar{E}$	Observed Magnetic Storm and Substorm* $\bar{E}$
	Range: 0.1-1 mV/m Value Used: 0.1 mV/m	Range: 1-5 mV/M Value Used: 2 mV/m
Ionosphere $B \approx 0.5 \times 10^{-4}$ Tesla	2 m/sec	40 m/sec
High Altitude (L-3) $B = 1.1 \times 10^{-6}$ Tesla	90 m/sec	$1.8 \times 10^3$ m/sec

\*Enhanced magnetic activity is estimated to occur about 25 percent of all time near solar maximum and about 10 percent of the time near solar minimum.

How significant drifts of this magnitude are depends on how much time the plasma spends in regions where the  $\bar{E} \times \bar{B}/B^2$  drifts are important. From discussions with MRC and the NRL (National Research Laboratory) groups, it appears that a specific segment of the plasma will spend periods of time greater than an hour in the equatorial region. If it spends just one hour,

it will drift through a distance  $1.8 \text{ km/sec} \times 3.6 \times 10^3 \text{ sec} = 6480 \text{ km} = 1.02 R_E$ . This corresponds to an angular translation of the order of  $1.02/3 \text{ radians} = 19.5^\circ$ . By comparison, neutral winds in the ionosphere generate angular drifts of the order of  $1^\circ/\text{hour}$ . Whether the translation is in latitude or longitude is determined by the direction of the electric field.

In addition to the translational motions of the plasma, the  $\bar{E} \times \bar{B}$  drift can contribute to plasma distortions which may contribute to subsequent plasma structuring. This is illustrated in Figure 4-2 where the variation of the penetrating component of  $\bar{E}$  results in the varying drift pattern.

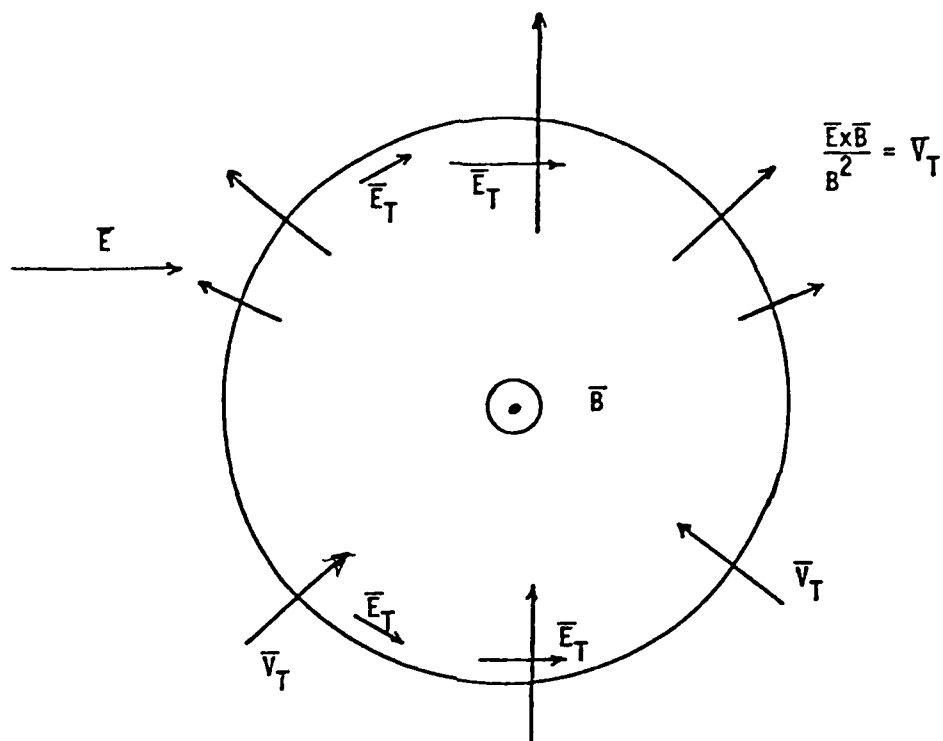
In summary the component of electric field tangent to the plasma boundary penetrates the plasma. The depth of penetration is most significant at higher altitudes and varies with position along the boundary. In the electromagnetic regime, where both plasma size and particle mean free path is much greater than the Larmor radius, the  $\bar{E} \times \bar{B}/B^2$  drift is important. Because of the geometrical dependence of  $\bar{E}$  (and the resulting geometrical dependence of the drift velocity), the motion resulting from this drift not only translates the plasma but also distorts its shape (contributes to internal structuring).

It is suggested that further investigations be made to see in detail if and how the time dependence of the distortion leads to the onset of structuring. Further, the  $\bar{E} \times \bar{B}$  drift will be larger still in the environment produced by multiple nuclear bursts. The implications of this for real battle situations on the structuring of the plume and the distortion of electromagnetic communications should be explored.

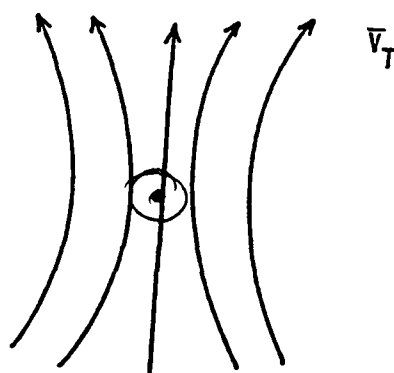
## 4.2 PERTURBATION OF THE NATURAL FIELD BY THE ARTIFICIAL PLASMA

### 4.2.1 Magnetic Signatures

Ground station magnetograms of the world wide magnetometer network have observed magnetic field perturbations persisting to late times following the various nuclear detonations. Magnetograms have been obtained for the post STARFISH period from the World Data Center A in Boulder, Colorado. Figure 4-3 shows the variation of the magnetic field at Honolulu and Guam following the STARFISH explosion. The zero level represents the level of the



(a) Inhomogeneous Velocity Distribution Resulting from Externally Produced  $\vec{E} \times \vec{B}$  Drifts



(b) Velocity Flow Lines Resulting from Externally Produced  $\vec{E} \times \vec{B}$  Drifts

Figure 4-2. Geometrical Dependence of  $\vec{E} \times \vec{B} / B^2$

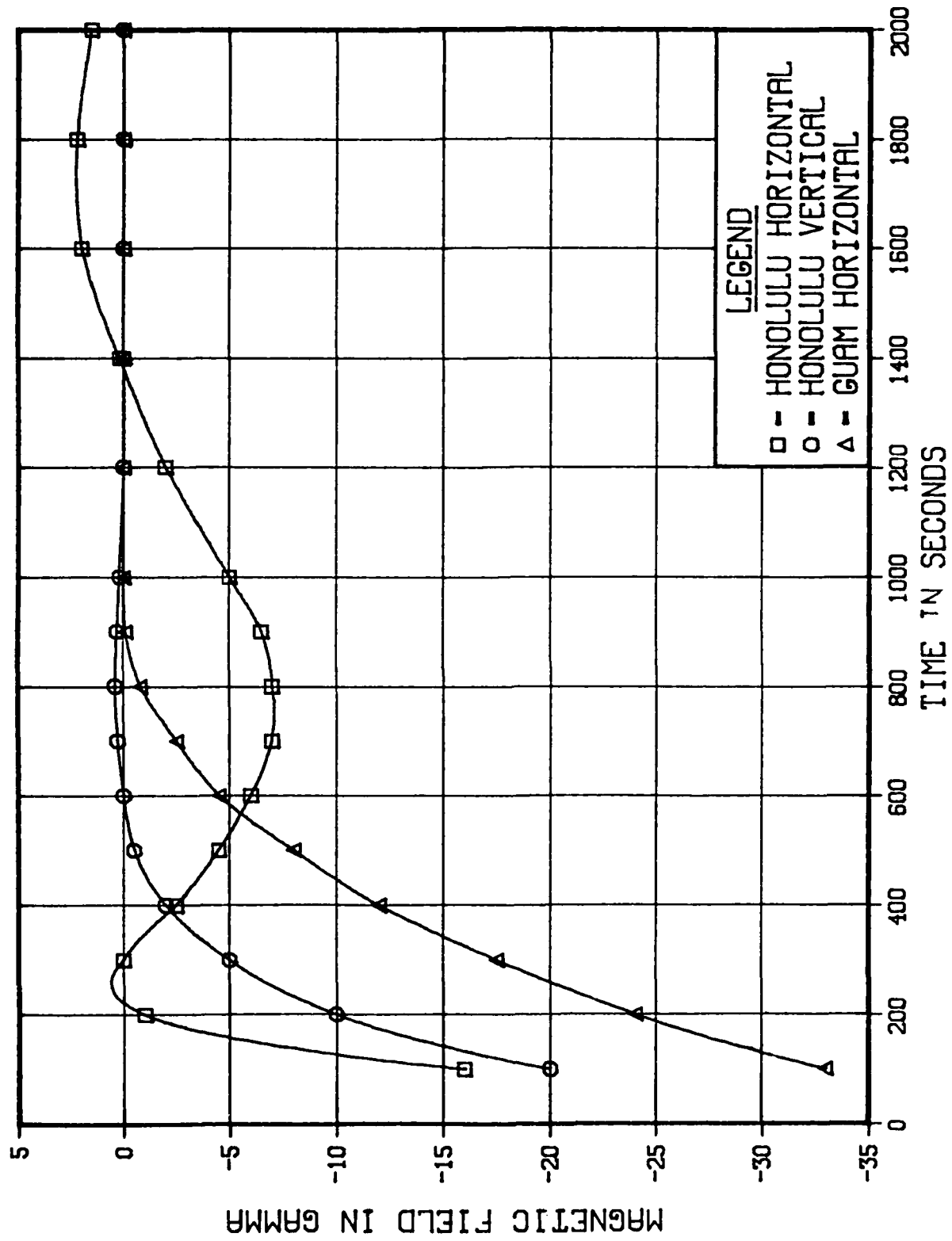


Figure 4-3. Observed Starfish Magnetic Field.

ambient field before and after the explosion. One notes that for late times ( $t > 500$  sec) a detectable signal persists. The magnetic field at late times is caused by the currents flowing within the plume. Computer codes which model the morphology of the plume can calculate the currents flowing within the plume and these currents can then be used to calculate the expected magnetic field. The calculated magnetic field for the model STARFISH detonation should then match the data obtained following the STARFISH burst. Thus, the magnetic field signature offers a test of the validity of the burst model. The magnetic field data can therefore provide an independent check on the total plume model although it cannot diagnose specific problems within the plume model.

To test the feasibility of calculating the magnetic field signature, MRC was asked to supply MDAC with information on the currents flowing within a plume. MRC first supplied MDAC with plots of the currents flowing with a typical 4 megaton plume, Figures 4-4, 4-5, and 4-6. Analysis of the plots found them to be considerably more complicated than expected. However, an approximation using wire loops at constant altitude to represent the currents, indicated that the field under the plume as calculated from the currents would be on the order of 10's to 100's of gamma. The complexity of the current patterns, however, indicated that the wire loops provided only a crude approximation. Thus, a more accurate procedure using direct volume integration over the current system was developed. MRC agreed to supply MDAC with a computer tape containing the current vectors at a grid of points. The method for calculating the magnetic field from the currents listed on the MRC computer tape are given below. (The format of the MRC computer tape is described in Appendix C.)

Given a current density,  $\bar{J}$ , the magnetic field  $\bar{B}$ , at a distance  $\bar{r}$ , from the observer is

$$\bar{B} = \frac{\mu_0}{4\pi} \int \frac{\bar{J} \times \bar{r}}{r^3} dV \quad (4-1)$$

(Note all equations are in MKS units.)



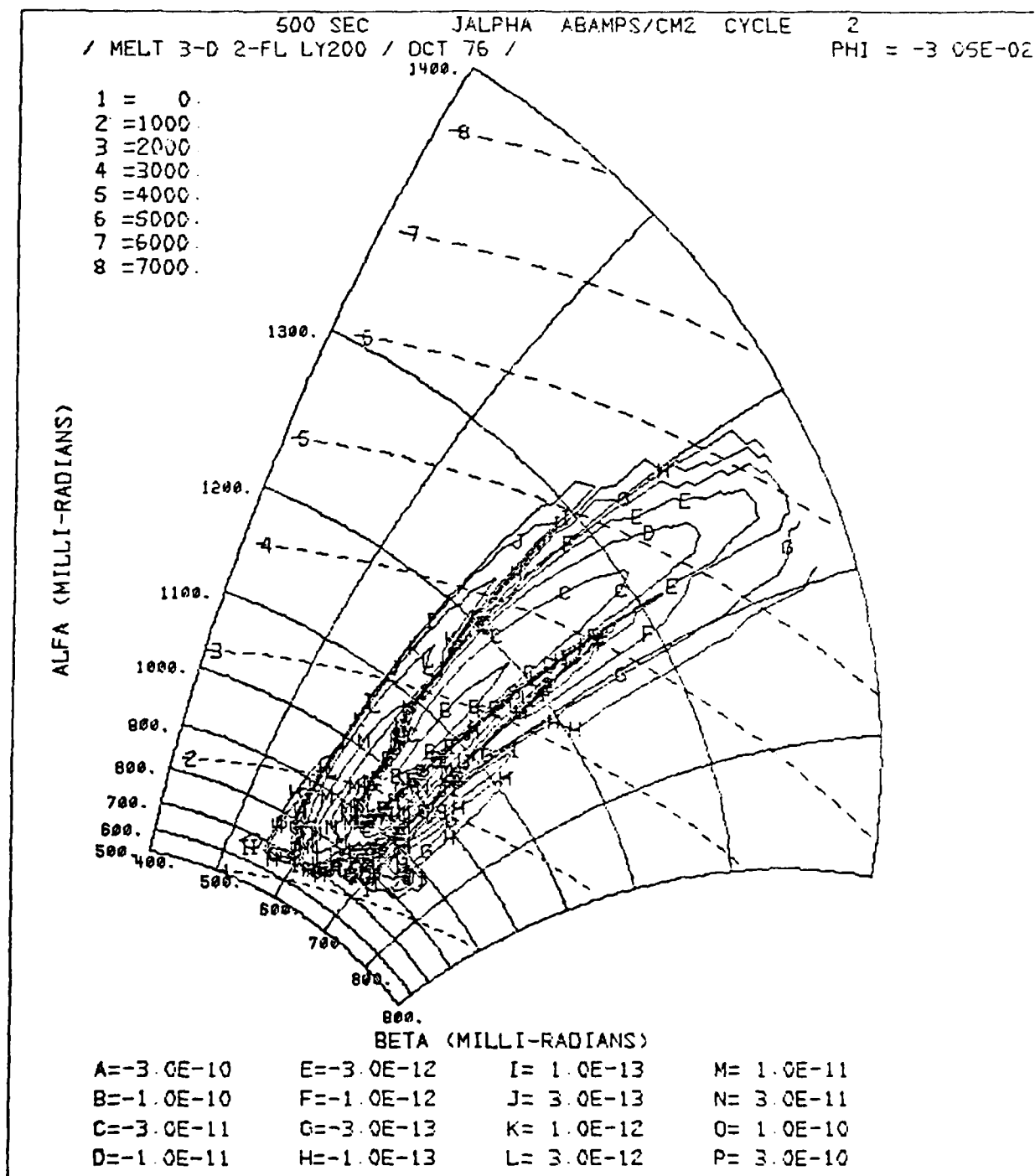


Figure 4-4. Currents Flowing with a Typical 4 Megaton Plume.

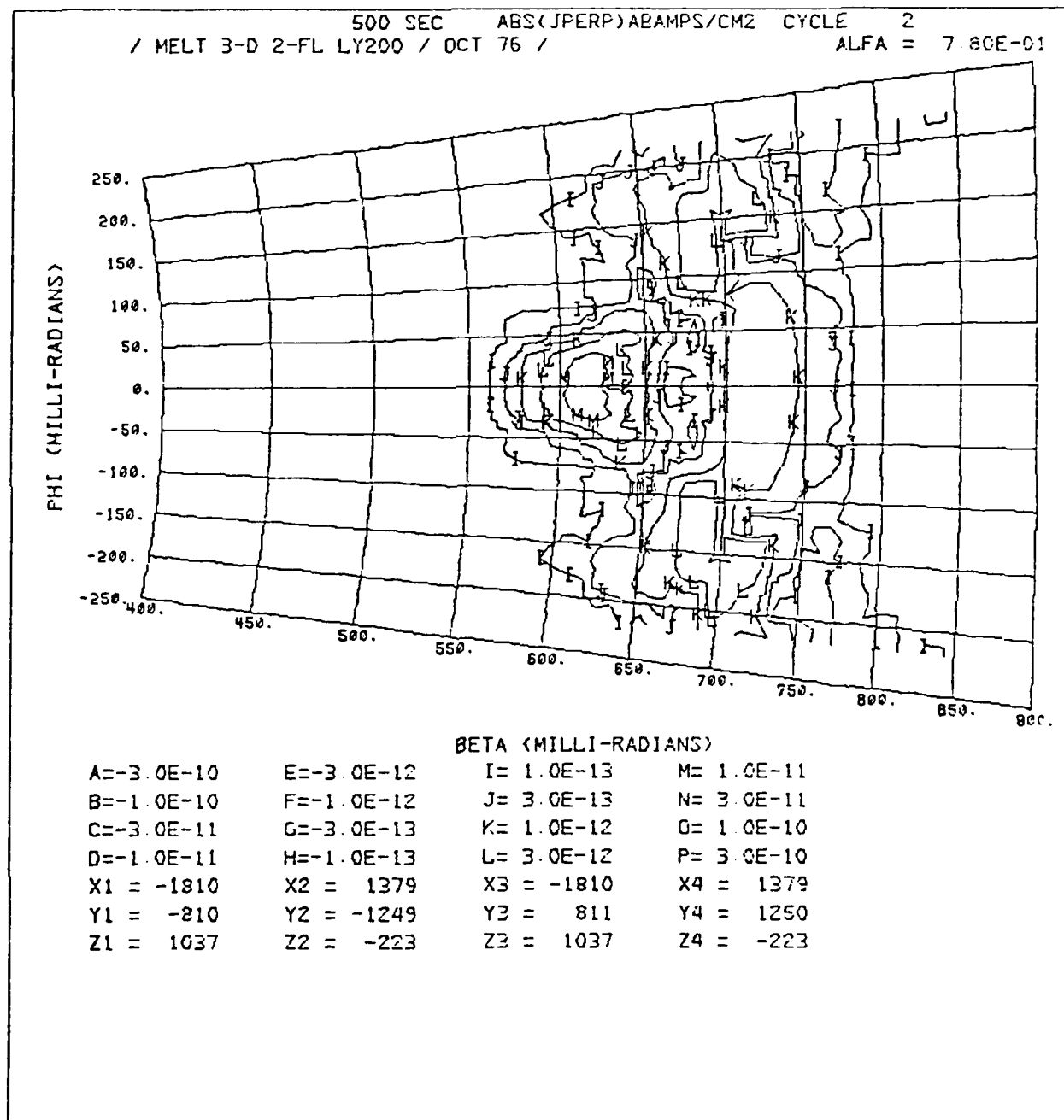


Figure 4-5. Currents Flowing with a Typical 4 Megaton Plume.

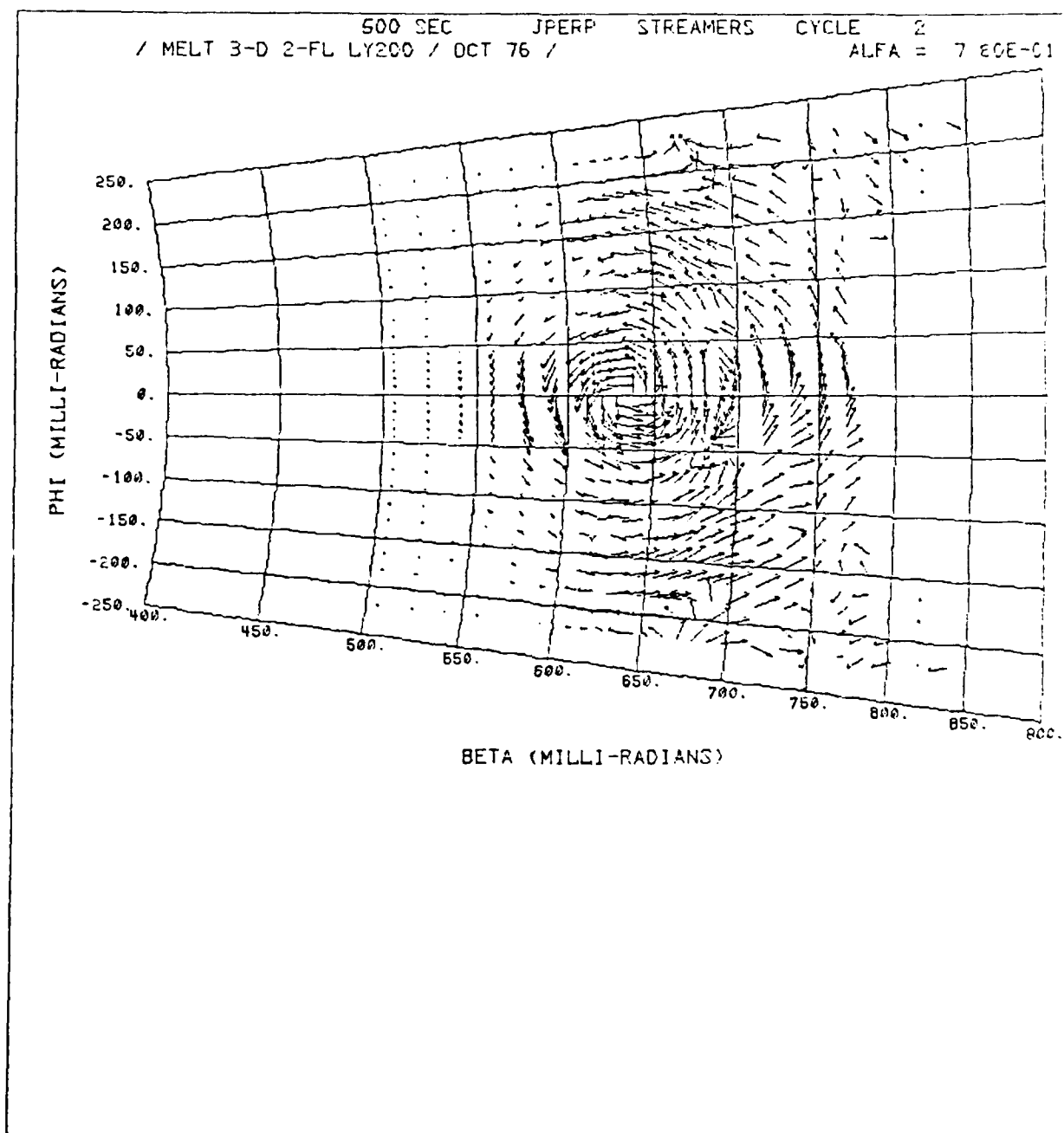


Figure 4-6. Currents Flowing with a Typical 4 Megaton Plume.

The integral is evaluated on the computer by using discrete volume elements  $\Delta V_i$ .

For each volume element,  $\Delta V_i$ , we associate a current density  $\bar{J}_i$ , where  $\bar{J}_i$  is the current density at the center of the volume element and  $\bar{r}_i$  is the distance to the center of the volume element. Thus,

$$\bar{B} = 10^{-7} \sum_{i=1}^N \frac{\bar{J}_i \times \bar{r}_i}{|\bar{r}_i|^3} \Delta V_i \quad (4-2)$$

A similar expression is available for the magnetic vector potential.

$$\bar{A} = 10^{-7} \sum_{i=1}^N \frac{\bar{J}_i}{|\bar{r}_i|} \Delta V_i \quad (4-3)$$

MRC supplied the current vectors in the  $\alpha$ ,  $\beta$  and  $\phi$  coordinate system with the currents spaced uniformly in  $\alpha$ ,  $\beta$  and  $\phi$ . The  $\alpha$  coordinate is along a magnetic field line, the  $\beta$  coordinate perpendicular to the magnetic field and in the plane containing the field line,  $\phi$  is perpendicular to  $\alpha$  and  $\beta$ .  $\phi$  is the standard spherical coordinate.  $\alpha$  and  $\beta$  are defined in terms of the spherical coordinates  $R$  and  $\theta$ , where  $R$  is the radius vector and  $\theta$  is the colatitude. The following equations relate  $\alpha$  and  $\beta$  to  $R$  and  $\theta$ .

$$\cos \alpha = \frac{R_E^2}{R^2} \cos \theta \quad (4-4)$$

$$\sin \beta = \sqrt{\frac{R_E}{R}} \sin \theta \quad (4-5)$$

$R_E$  is the radius of the earth (6371 km).

The quickest and simplest method of evaluating the integral for the Biot Savart law (Equations 4-2 and 4-3) is to perform the integral in cartesian coordinates. The volume element in cubic meters is given by the expression

$$\begin{aligned} \Delta V = & \frac{\Delta \phi R_e^3}{3} \left\{ \frac{1}{\sin^6 \beta_1} \left[ -\cos \theta + \cos^3 \theta - \frac{3}{5} \cos^5 \theta + \frac{1}{7} \cos^7 \theta \right]_{\theta_1}^{\theta_2} \right. \\ & + \left[ \frac{2}{5} \left( \frac{\cos \theta}{\cos \alpha_1} \right)^{3/2} \cos \theta \right]_{\theta_1}^{\theta_3} - \left[ \frac{2}{5} \left( \frac{\cos \theta}{\cos \alpha_2} \right)^{3/2} \cos \theta \right]_{\theta_2}^{\theta_4} \\ & \left. + \frac{1}{\sin^6 \beta_2} \left[ \cos \theta - \cos^3 \theta + \frac{3}{5} \cos^5 \theta - \frac{1}{7} \cos^7 \theta \right]_{\theta_3}^{\theta_4} \right\} \end{aligned} \quad (4-6)$$

The symbols are defined in Figure 4-7. A complete derivation is given in Appendix D. Once given the volume element, the  $J_\alpha$  and  $J_\beta$  components must first be transformed into cartesian coordinates. This is most easily accomplished by first transforming  $J_\alpha$  and  $J_\beta$  into spherical coordinates  $J_\theta$  and  $J_r$ .

$J_\alpha$  can be split into a component in the  $r$  direction,  $J_{\alpha r}$ , and a component in the  $\theta$  direction,  $J_{\theta}$ . Since a line in the  $\alpha$  direction has the equation

$$R = R_e \frac{\sin \theta}{\sin^2 \beta_1} \quad (4-7)$$

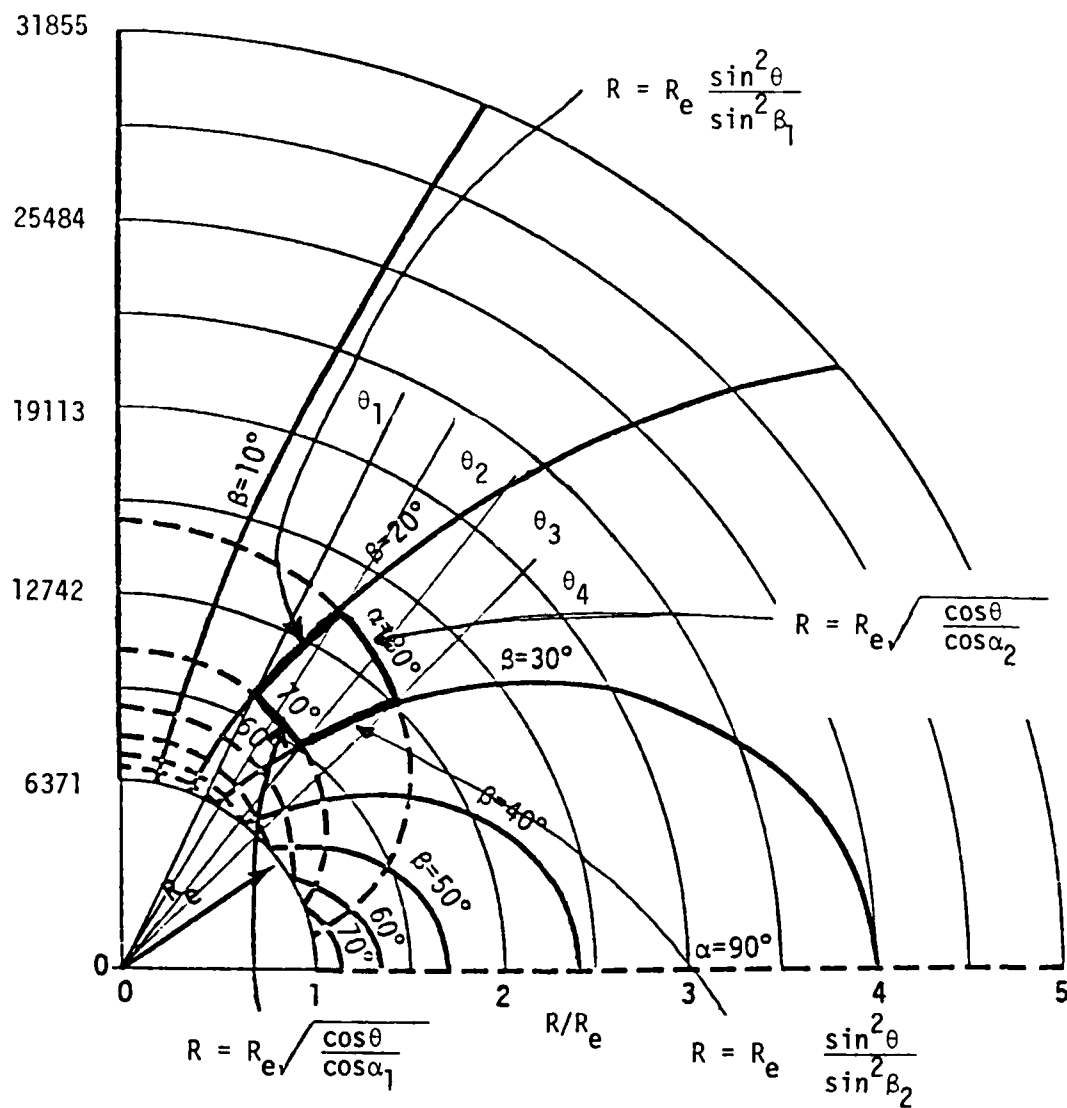


Figure 4-7. The  $(\alpha, \beta)$  coordinates for the field-aligned dipole coordinate system far from the earth.

and since

$$\frac{J_{\alpha r}}{J_{\alpha \theta}} = \frac{dR}{R d\theta} \quad (4-8)$$

it can be shown that

$$J_{\alpha r} = 2 \frac{\cos \theta}{\sin \theta} J_{\alpha \theta} \quad (4-9)$$

Furthermore, since

$$J_{\alpha}^2 = J_{\alpha r}^2 + J_{\alpha \theta}^2 \quad (4-10)$$

Substituting Equation (4-9) into Equation (4-10) and solving for  $J_{\alpha \theta}$  one gets that

$$J_{\alpha \theta} = \frac{\sin \theta}{\sqrt{1 + 3 \cos^2 \theta}} J_{\alpha} \quad (4-11)$$

and

$$J_{\alpha r} = \frac{2 \cos \theta}{\sqrt{1 + 3 \cos^2 \theta}} J_{\alpha} \quad (4-12)$$

A similar procedure for the  $\beta$  component  $J_{\beta}$  gives that

$$J_{\beta \theta} = \frac{2 \cos \theta}{\sqrt{1 + 3 \cos^2 \theta}} J_{\beta} \quad (4-13)$$

and

$$J_{\beta r} = \frac{-\sin\theta}{\sqrt{1 + 3\cos^2\theta}} J_{\beta} \quad (4-14)$$

Since

$$J_r = J_{\alpha r} + J_{\beta r}$$

$$\text{and} \quad J_{\theta} = J_{\alpha\theta} + J_{\beta\theta} \quad (4-15)$$

One can combine Equations (4-12) and (4-14) and combining Equations (4-11) and (4-13) to give

$$J_r = \frac{2 \cos \theta J_{\alpha} - \sin \theta J_{\beta}}{\sqrt{1 + 3 \cos^2 \theta}} \quad (4-16)$$

$$J_{\theta} = \frac{2 \cos \theta J_{\beta} + \sin \theta J_{\alpha}}{\sqrt{1 + 3 \cos^2 \theta}} \quad (4-17)$$

The final transformation to cartesian coordinates is

$$J_x = \cos\phi (\sin\theta J_r + \cos\theta J_{\theta}) - \sin\phi J_{\phi} \quad (4-18)$$

$$J_y = \sin\phi (\sin\theta J_r + \cos\theta J_{\theta}) + \cos\phi J_{\phi} \quad (4-19)$$

$$J_z = \cos\theta J_r - \sin\theta J_{\theta} \quad (4-20)$$

The components of currents,  $J_{\alpha}$ ,  $J_{\beta}$ ,  $J_{\phi}$  given by MRC on the magnetic tapes are not all given at the center of the volume element. Instead some



are given at the center of the faces of the cell. Appropriate interpolation schemes are used to calculate  $J_\alpha$ ,  $J_\beta$  and  $J_\phi$  at the center of the volume element. These volume centered coordinates are then converted to cartesian coordinates using Equations (4-16) through (4-20). These currents along with the element calculated using Equation (4-6) are used in Equations (4-2) and (4-3) to calculate  $\bar{A}$  and  $\bar{B}$  at a given point and time.

Table 4-2 lists some of the results from the current integration. All values are along the  $\phi = 0$  plane. The magnitudes of the calculated fields are very similar to the STARFISH data set. An exact comparison cannot be made since the calculated fields are for the model 4 megaton burst and the data are for STARFISH. Furthermore, the effect of the induced telluric currents have not been included. Also note that the burst data were available only at 500 sec intervals. It is therefore not possible to determine if the large fluctuations in the calculated magnetic field values (intuitively, monotonic decay might be expected) are "real" or if there is a problem with the codes.

Table 4-2  
CALCULATED MAGNETIC FIELD IN GAMMA  
Typical 4 Megaton Burst

Colatitude	Altitude	Time			
		500	1000	1500	2000
30	0	9.9	5.7	6.8	13
35	0	44	27	11	36
40	0	49	102	5	60
45	0	24	42	18	34
50	0	13	19	4	16
5	0	0.56	0.52	0.23	0.89
90	0	0.75	0.35	1.12	2.47
5	30,000	0.007	0.012	0.027	0.035

Maximum  $E_I = \partial A / \partial t \approx 0.2$  mV/m

The maximum variation of the vector magnetic potential gives a self induction electric field within the cloud of 0.2 mV/m which is on the borderline of being negligible.

Thus, a method has been developed and tested which permits the calculations of the magnetic field from a model plume at any magnetometer location. These calculations can be used to check the magnetic field calculated by the computer model against observational data. The observational data for STARFISH is well defined and thus a calculation with the STARFISH currents is indicated when the STARFISH currents become available.

#### 4.2.2 Multiburst Effects

It appears clear from the preceding sections that interaction of multiple high altitude bursts can occur through mechanisms other than magnetohydrodynamic waves and shocks. High altitude fireballs which are largely contained by the magnetic field will be sensitive to any changes in the magnetic field occurring near the burst point. Remotely occurring, high altitude bursts, may be able to produce sufficient changes in the magnetosphere to directly produce, or indirectly precipitate magnetic field fluctuations similar to the naturally occurring magnetic substorms.

Large displacements of the magnetic field can occur in the immediate vicinity of a high altitude burst point. Some idea of the magnitude of this displacement can be obtained by comparing the energy content of the ambient field with energy content of the ionized atmosphere and bomb debris. Depending on the burst altitude and weapon yield, displacement of the order of several earth radii should be expected. This, coupled with the magnetohydrodynamic wave and shock effects, can yield complicated structure and motion in existing and subsequent fireballs.

Any changes in the magnetosphere influencing the structure of natural plasma, in the current systems and in the ionosphere, will have an effect on both earth based and satellite communication systems. To properly evaluate performance of such systems, the importance of the influence of large yield multiple bursts in the magnetosphere must be understood.

## Section 5

### CONCLUSIONS AND RECOMMENDATIONS

The objectives of this study were to approach the problem of plasmas artificially injected into the high altitude ionosphere from the viewpoint of their interaction with the ambient electromagnetic field environment (e.g., those associated with the magnetospheric substorm and the daily wobble of the earth's dipole magnetic field) and in a selfconsistent manner to examine the mutual influence of the plasma and the electromagnetic field. It was found that the natural electric fields contribute to both the drift motion and structuring of the plasma. To do this, the principal sources of the natural electric field were identified, and a model of the most persistent field (resulting from the daily variation of the magnetospheric magnetic field) was developed. The model describes the total electric field which includes a component produced by the plasma as it responds to the field induced by the wobbling dipole.

The approach taken in deriving this model is outlined in the proposal for this work. The model was made sufficiently flexible to allow for its expansion to include contributions from other sources to the extent that they influence the structure and motion of the various magnetospheric current systems. Some sources of the natural electric fields are identified in Table 2-1; those which can readily be modeled with our approach are indicated in the table.

The natural electric fields in the magnetosphere have periods of the order of 0.25 hour, or more, and are thus very low frequency in character. As a result, they penetrate the plasmas of interest here with very little loss of energy (i.e., have large skin depths). The estimates of plasma properties were performed under several simplifying assumptions; the range of values used are typical of the cases of interest to this study. The dominant feature of the problem is the extremely low frequency range of the electromagnetic waves. The normal variations of the other parameters (such as the collision frequencies) with respect to the values used in the present work do not alter the conclusions appreciably.

In addition to developing the electric field model itself, the possible influence of this electric field on the motion and structure of an artificially generated plasma was investigated. Although preliminary in nature the results of these calculations indicate that the plasma can be influenced by this field; the  $\bar{E} \times \bar{B}$  drift not only contributes to the general motion of the plasma but can also influence internal structuring of the plasma. High density plasmas in the ionosphere are expected to be influenced only slightly by the smaller natural electric field there. As these plasmas expand outward along magnetic field lines, the penetration of the electric field increases and the decrease in  $B$  (i.e.,  $\bar{E} \times \bar{B} / B^2$  increases) produces a significant plasma drift velocity. The penetration of  $\bar{E}$  is anisotropic in nature and depends on the detailed structure of the plasma. The plasma is expected to drift with respect to the magnetic field lines, the variation in drift velocities throughout this region contributing to the internal structuring of the plasma.

The conditions in the plasma which allow penetration of the external electric field are also those under which the assumption that magnetic field lines are essentially equipotentials becomes poor. The breakdown of this condition allows the less dense plasmas, in the extended region of the magnetically contained plasma plume, to act more or less independently of the denser, low altitude regions. Models of plasma dynamics in the magnetosphere which depend on the "field line coupling" assumption cannot correctly describe plasma motions in the regimes of interest here.

Although not included in the original work statement, work was also performed on the perturbations to the ambient fields resulting from the presence of the artificial plasma. The result is the evaluation of the magnetic signatures which could be observed by earth based magnetometer stations. The results for a model high altitude nuclear weapon burst are compared with the available data. These calculations are based on current density data within the late time fireballs, as calculated by the MRC MICE and MELT codes. The results are compared to magnetometer observations during actual bursts. The results are positive and indicate that this technique can be useful in the evaluation of the performance of hydrodynamic codes such as

MICE and MELT. Further extension of these techniques to evaluate the effects of high altitude nuclear weapon detonations on the magnetosphere may prove very useful in studies of communication, satellite, and ballistic missile defense system performance under nuclear attack. Multiple burst effects would be one area where this technique could be applied. Also the techniques used for quantitatively determining induced electric fields can be extended for use in the auroral regions and to higher latitudes generally and can be applied to the multiburst environment.

## REFERENCES

- Adamson, D., C. L. Fricke, S. A. T. Long, W. F. Landon, and D. L. Ridge, Preliminary Analysis of NASA Optical Data Obtained in Barium Ion Cloud Experiment of September 21, 1971. J. Geophys. Res., 78, p 5769, 1973.
- Barrish, F. D., and J. G. Roederer. Experimental Test of Magnetospheric Model. J. Geophys. Res., 78, p 5795, 1973.
- Francis, S. H., and F. W. Perkins. Determination of Striation Scale Sizes for Plasma Clouds in the Ionosphere. J. Geophys. Res., 80, 22, p 3111, 1975.
- Hones, Jr., E. W., and J. E. Bergeson. Electric Field Generated by a Rotating Magnetized Sphere, J. Geophys. Res., 70, p 4951, 1965.
- Northrop, T. G. The Adiabatic Motion of Charged Particles, John Wiley and Sons (Interscience), New York, 1963.
- Olson, W. P., and K. A. Pfitzer. Magnetospheric Field Modeling, McDonnell Douglas Astronautics Company Annual Scientific Report to AFOSR, January 1977.
- Olson, W. P., K. A. Pfitzer, and G. J. Mroz. Modeling the Magnetospheric Magnetic Field, to be published in the American Geophysical Union Geophysical Monograph, 1979.

## Appendix A

### DERIVATION OF PLASMA CHARACTERISTICS IN AN EXTERNAL MAGNETIC FIELD

Maxwell's equations in MKS rationalized units are:

$$\nabla \times \bar{H} = \bar{J} + \epsilon_0 \frac{\partial \bar{E}}{\partial t} \quad (A-1)$$

$$\nabla \times \bar{E} = - \frac{\partial \bar{B}}{\partial t} \quad (A-2)$$

$$\nabla \cdot \bar{E} = \frac{\rho}{\epsilon_0} \quad (A-3)$$

$$\nabla \cdot \bar{B} = 0 \quad (A-4)$$

Divergence of Equation A-1, using Equation A-3 gives

$$\nabla \cdot \bar{J} + \frac{\partial \rho}{\partial t} = 0 \quad (A-5)$$

the continuity of charge equation.

For a plasma in a magnetic field and an alternating low frequency electric field

$$\bar{J} = \sigma \bar{E}$$

and  $\rho = -\epsilon_0 \nabla \cdot (\chi \bar{E})$ .

Using  $e^{i\omega t}$  time dependence in Equation A-5 gives

$$i\omega\epsilon_0 X = \sigma.$$

$$\text{Let } \sigma = \sigma_r + i\sigma_i, \quad X = X_r + iX_i$$

$$\text{then } X_r = \frac{\sigma_i}{\omega\epsilon_0} \quad \text{and} \quad X_i = \frac{-\sigma_r}{\omega\epsilon_0}$$

In terms of  $X_r$ ,  $\sigma_r$  one has

$$\nabla \times \vec{H} = \sigma_r \cdot \vec{E} + i\omega\epsilon_0(1 + X_r) \vec{E}$$

$$\nabla \times \vec{E} = -i\omega\vec{B}$$

$$\nabla \cdot (\epsilon_0(1 + X_r - i \frac{\sigma_r}{\omega\epsilon_0}) \vec{E}) = 0$$

$$\nabla \cdot \vec{B} = 0.$$

We are interested in low frequency  $\omega \ll \nu \ll \omega_c$  and long wavelength electric fields.

Using Langevin's equation (neutrals are assumed approximately at rest)

$$m_e \frac{d\vec{V}_e}{dt} + m_e \nu_{en} \vec{V}_e + m_e \nu_{ei} (\vec{V}_e - \vec{V}_i) = e(\vec{E} + \vec{V}_e \times \vec{B}) \quad (\text{A-6})$$

$$M_i \frac{d\vec{V}_i}{dt} + M_i \nu_{in} \vec{V}_i + M_i \nu_{ie} (\vec{V}_i - \vec{V}_e) = e(\vec{E} + \vec{V}_i \times \vec{B}) \quad (\text{A-7})$$



where the subscripts e, i refer to electron, and positive ion properties, respectively,

$\nu_{en}$  = collision frequency of electrons with the neutrals

$$= 2.6(10^4) R^2 N_n T_e^{1/2}$$

$R \approx$  classical radius of the neutrals  $\sim 10^{-10}$  meter

and  $T_e$  = electron temperature ( $^{\circ}\text{K}$ ) = 5,500 $^{\circ}\text{K}$  (1/2 e v).

Taking  $N_n = 10^{12}/\text{cc} = 10^{18}/\text{m}^3$ ,  $\nu_{en} \approx 2(10^4) \text{ sec}^{-1}$ . For plasma in equatorial regions ( $L=3$ ), the density of the neutral species is negligible and  $\nu_{en} \approx 0$ .

For the collision frequency of ions with neutrals, we use

$$\nu_{in} = \frac{6.1(10^2) R^2}{\sqrt{W}} N_n T_i^{1/2}, \text{ where } W \text{ is molecular weight of ions.}$$

Thus,  $\nu_{in} = 1.1(10^2) \text{ sec}^{-1}$  in the ionosphere (for  $N_n = 10^{18}/\text{m}^3$ )

and  $\nu_{in} = 0$  in the equatorial regions.

The collision frequency of electron due to ions

$$\nu_{ei} \approx 3.6(10^{-6}) N_i T_e^{-3/2} \log_e \left( \frac{1.23(10^7) T_e^{3/2}}{N_e^{1/2}} \right)$$

As  $T_e \approx 5,500^\circ\text{K}$ ,  $N_i \approx N_e \approx 10^6/\text{cc} = 10^{12}/\text{m}^3$

$\nu_{ei} \approx 1.4(10^2) \text{ sec}^{-1}$  in the boundary regions of the plasma. In the center of plasma,  $N_i = N_e \approx 10^{14}/\text{m}^3$  and  $\nu_{ei} \approx 10^4 \text{ sec}^{-1}$ .

For the collision frequency of ions with the electrons,

$$\nu_{ie} \approx \frac{m_e}{M} \nu_{ei}.$$

Now,  $m_e/m_p = 5.44(10^{-4})$  and  $m_e/m_{O^+} = 3.37(10^{-5})$ , where  $m_p$ ,  $m_{O^+}$  is the mass of the proton and oxygen ion, respectively.

So, for the low density plasma, e.g., boundary regions of the plasma,

$N_i \approx N_e = 10^{12} \text{ m}^{-3}$ ,  $\nu_{ei} = 1.4(10^2) \text{ sec}^{-1}$ , we have  $\nu_{ie}(H^+) = 7.62(10^{-2})\text{sec}$  and  $\nu_{ie}(O^+) \approx 4.72(10^{-3})\text{sec}$ . For the high density plasma, e.g., center of the plume,  $N_i \approx N_e = 10^{14} \text{ m}^{-3}$  and  $\nu_{ei} \approx 10^4 \text{ sec}^{-1}$ , we have  $\nu_{ie}(H^+) = 5.44 \text{ sec}^{-1}$ ,  $\nu_{ie}(O^+) = 0.337 \text{ sec}^{-1}$ .

Solving Equations A-6 and A-7, using  $\omega \ll \omega_c$ ,  $\nu$ 's and  $\frac{d}{dt} = \frac{\partial}{\partial t} + \mathbf{V} \cdot \nabla$ ; also

letting  $\omega_{ce} = \frac{eB}{m_e}$ ,  $\omega_{ci} = \frac{eB}{M_i}$ , gives the Pederson components of the conductivity

$$(\sigma_{xx})_r = (\sigma_{yy})_r = \frac{n_e e^2}{m_e} \frac{(\nu_{en} + \nu_{ei})}{(\nu_{en} + \nu_{ei})^2 + (\omega_{ce}^2)}$$

$$- \frac{n_i e^2 \nu_{ie}}{m_e} \left[ \frac{(\nu_{in} + \nu_{ie})(\nu_{en} + \nu_{ei}) + \omega_{ci} \omega_{ce}}{[(\nu_{en} + \nu_{ei})^2 + \omega_{ce}^2][(\nu_{in} + \nu_{ie})^2 + \omega_{ci}^2]} \right]$$

$$\begin{aligned}
& + \frac{n_i e^2}{m_i} \frac{(v_{in} + v_{ie})}{(v_{in} + v_{ie})^2 + \omega_{ci}^2} \\
& - \frac{n_e e^2 v_{ei}}{m_i} \left[ \frac{(v_{in} + v_{ie})(v_{en} + v_{ei}) + \omega_{ci} \omega_{ce}}{[(v_{en} + v_{ei})^2 + \omega_{ce}^2][(v_{in} + v_{ie})^2 + \omega_{ci}^2]} \right]
\end{aligned}$$

The Hall components of the conductivity are given by

$$\begin{aligned}
(\sigma_{xy})_r &= -(\sigma_{yx})_r = \frac{n_e e^2}{m_e} \frac{\omega_{ce}}{(v_{en} + v_{ei})^2 + \omega_{ce}^2} \\
& - \frac{n_i e^2 v_{ie}}{m_e} \left[ \frac{\omega_{ce}(v_{in} + v_{ie}) - (v_{en} + v_{ei}) \omega_{ci}}{[(v_{ei} + v_{en})^2 + \omega_{ce}^2][(v_{in} + v_{ie})^2 + \omega_{ci}^2]} \right] \\
& - \frac{n_i e^2}{m_i} \frac{\omega_{ci}}{(v_{in} + v_{ie})^2 + \omega_{ci}^2} \\
& + \frac{n_e e^2 v_{ei}}{m_i} \left[ \frac{\omega_{ci}(v_{en} + v_{ei}) - \omega_{ce}(v_{in} + v_{ie})}{[(v_{ei} + v_{en})^2 + \omega_{ce}^2][(v_{in} + v_{ie})^2 + \omega_{ci}^2]} \right]
\end{aligned}$$

In the ionosphere  $B \approx 0.5(10^{-5})$  Tesla.

$$\begin{aligned}
\omega_{ce} &\approx 9(10^5) \text{ sec}^{-1}, \quad \omega_{ci} \text{ (for } O^+) \approx 3(10^2) \text{ sec}^{-1}, \quad \omega_{ci}(H^+) \\
&= 4.9(10^3) \text{ sec}^{-1}.
\end{aligned}$$

In the equatorial region (L=3)  $B \approx 1.1(10^{-6})$  Tesla

$$\omega_{ce} \approx 2(10^5) \text{ sec}^{-1}, \quad \omega_{ci} \text{ (for } H^+) \approx 1.1(10^2) \text{ sec}^{-1}, \quad \omega_{ci}(O^+) = 6.74 \text{ sec}^{-1}.$$

In the ionosphere  $\nu_{in} < \nu_{en}$ . Assuming  $O^+$  species only,  $\omega_{ci} \sim \nu_{in}$ ,  $\omega_{ce} \gg \nu_{en}$ .

For the low density regime ( $N \sim 10^{12} \text{ m}^{-3}$ ),  $\nu_{ei} \sim \nu_{in}$ ,  $\nu_{ie} \ll \nu_{in}$  and so

$\omega_{ce} \gg \nu_{en} > \nu_{in} \sim \omega_{ci} \sim \nu_{ei} \gg \nu_{ie} > \omega$ . For the high density regime

( $N \sim 10^{14} \text{ m}^{-3}$ ),  $\nu_{ei} \sim \nu_{en}$ ,  $\nu_{ie} < \nu_{in}$ , and so  $\omega_{ce} \gg \nu_{en} \sim \nu_{ei} > \nu_{in} \sim \omega_{ci}$

$> \nu_{ie} > \omega$ , the Pedersen conductivity becomes approximately

$$(\sigma_{xx})_r \approx \frac{N_i e^2 (\nu_{in} + \nu_{ie})}{m_i [\omega_{ci}^2 + (\nu_{in} + \nu_{ie})^2]} \approx \frac{N_{ie}^2}{m_i} \cdot \frac{\nu_{in}}{\nu_{in}^2 + \omega_{ci}^2} = \begin{matrix} \text{Low Density} \\ 1.05(10^{-3}) \text{ mho/m} \\ \text{High Density} \\ 1.05(10^{-1}) \text{ mho/m} \end{matrix}$$

In the equatorial region (high altitude) in the boundary of the plasma ( $N_i = 10^{12}/\text{m}^3$ , the Hall conductivity is  $(\sigma_{xy})_r \sim 1.4(10^{-3}) \text{ mho/m}$ . In denser regions ( $N_i \approx 10^{14}/\text{m}^3$ ) of plasma, the Hall conductivity is  $(\sigma_{xy})_r \sim 0.15 \text{ mho/r}$ .

The Hall conductivity is smaller than the Pedersen conductivity for the regimes of interest here. Thus, in the ionosphere the skin depth parallel to the electric field, which is perpendicular to the magnetic field, is

$$\delta \sim \sqrt{\frac{1}{\omega \mu_0 \sigma_{xx}}} = \begin{matrix} 3.3(10^3) \text{ km at plasma boundary} \\ 3.3(10^2) \text{ km in dense regions} \end{matrix}$$

where we used  $\omega \approx 2\pi/3600 \cdot 24 \text{ sec} = 7.3(10^{-5}) \text{ sec}^{-1}$ , as the characteristic time dependence for the E field at quiet times.

Thus, the electric field enters well into the boundary layer of the plasma.

In the equatorial regions, for  $L=3$ , where there are no neutrals and where  $O^+$  ions are assumed dominant ( $\nu_{en} \sim \nu_{in} \sim 0$ ).

Low Density Plasma Regime  $\omega_{ce} \gg \nu_{ei} > \omega_{ci} \gg \nu_{ie} \gg \omega$

High Density Plasma Regime  $\omega_{ce} \gg \nu_{ei} \gg \omega_{ci} \sim \nu_{ie} \gg \omega$

$$\sigma(\text{Pedersen}) = \frac{n_i e^2}{m_i} \left( \frac{\nu_{ie}}{\nu_{ie}^2 + \omega_{ci}^2} \right) \begin{array}{l} \approx 1(10^{-6}) \text{ mho/m} = \text{the boundary regions} \\ \approx 0.72 \text{ mho/m} = \text{the dense regions} \end{array}$$

$$\text{The skin depth, } \delta \approx \begin{cases} 1.1(10^5) \text{ km at the boundary} \\ 1.2(10^4) \text{ km at the denser plasma.} \end{cases}$$

This was done using  $\omega = 7.3(10^{-5})$  (24 hour period) as the characteristics time dependence of the  $\bar{E}$  field during magnetic storms. Again the electric field enters well into the boundary layer of the plasma.

Appendix B  
DERIVATION OF PLASMA DRIFT VELOCITIES

To obtain the expressions for the significant particle drift velocities, we consider the following equations of motion:

$$\frac{\partial(n_e V_e)}{\partial t} + \nabla \left( \frac{KT_e n_e}{m_e} \right) - \frac{e}{m_e} (E + V_e \times B) n_e = v_{ei}(V_e - V_i) n_e + v_{en}(V_e) n_e$$

$$\frac{\partial(n_i V_i)}{\partial t} + \nabla \left( \frac{KT_i n_i}{M_i} \right) + \frac{e}{M_i} (E + V_i \times B) n_e = v_{ie}(V_i - V_e) n_e + v_{in} V_i n_e$$

We can neglect  $\partial/\partial t$  terms because of small temporal variation, and neglect  $v_{in}$ ,  $v_{en}$  in the equatorial regions.

Assume small charge displacement  $n_e \approx n_i$ ,  $V_e = V_i$ , and  $KT_e = KT_i$ .

Thus, for each species  $KT_e \frac{\nabla n}{n} + q(E + V \times B) \approx 0$ , where  $q = \pm e$ .

Taking the cross product of  $\vec{B}$  and the above, gives

$$KT_e \frac{\nabla n \times B}{n} + q E \times B + q (V \times B) \times B = 0.$$

But  $(V \times B) \times B = (V_{\perp} \times B) \times B = V_{\perp} B^2 + (V_{\perp} \cdot B) B,$

where  $V_{\perp}$  is component of  $V$  in plane perpendicular to  $B$ .

$$\text{Now } V_{\perp} \cdot \bar{B} = 0, \text{ and } V_{\perp} = \frac{KT_e \nabla n \times \bar{B} / n}{qB^2} + \frac{E \times \bar{B}}{B^2}.$$

Note that the  $E \times \bar{B}$  term is independent of the sign of  $q$  (i.e., common drift for each species) while  $\nabla n \times \bar{B} / qB^2$  produces a drift in different direction for each species.

Since  $\nabla n$  is radial,  $\nabla n \times \bar{B}$  is azimuthal;  $\bar{E}$  is also azimuthal (high at top and bottom, zero in middle), hence  $E \times \bar{B} / B^2$  is radial. That is, the  $E \times \bar{B} / B^2$  drift is not in the same direction as  $\nabla n \times \bar{B}$ ; and as a result, a small field  $E$  can lead to a slow, steady effect and cause significant translational motions of the plasma.

(Note that  $E \times \bar{B} / B^2 = 1.8 \text{ km/sec}$  for  $E = 2(10^{-3}) \text{ V/m}$  and  $B = 1.1(10^{-6}) \text{ Tesla}$ .)

Appendix C  
CURRENT DENSITY MAGNETIC TAPE FORMAT

The data tape of current vectors supplied to MRC is an unlabeled, 1600 BPI, binary tape written by the CDC Cyber Record manager using S record type and C type blocking. The format for the tape is given below.



Record 1 - Header Record

NCYCLE, TIME, TION, NREC, LENGTH1, MREC, LENGTH2, JMXA, JMXB,  
JMPX

Record 2 - Grid Record

(AKB(I), I=0, JMXA), (BKB(I), I=0, JMXB), (PKB(I), I=0, JMPX),  
(DAKB(I), I=1, JMXA), (DBKB(I), I=1, JMXB), (DPKB(I), I=1, JMPX)

Stick Records ("NREC" Records of "LENGTH1" words each)

(BKV(I), I=1,4), (PKV(I), I=1,4), (AKB(I), I=0, JMXA),  
(CJA(I), I=0, JMXA)

Vertex Records ("MREC" Records of "LENGTH2" words each)

BV, PV, (AKC(I), I=1, JMXA), (CJB(I), I=1, JMXA),  
(CJP(I), I=1, JMXA)

## DEFINITIONS

NCYCLE	MELT master cycle number
TIME	Simulation time (sec)
TION	Ion fluid time for consistency checks in MELT (sec)
NREC	Number of stick records - $JM XB * JM XP$
LENGTH1	Number of 60-bit words in each stick record = $10 + 2 * JM XA$
MREC	Number of vertex records = $(JM XB + 1) * (JM XP + 1)$
LENGTH2	Number of 60-bit words in each vertex record = $2 + 3 * JM XA$
JM XA	Number of grid cells in $\alpha$ -direction
JM XB	Number of grid cells in $\beta$ -direction
JM XP	Number of grid cells in $\phi$ -direction
AKB(I)	Array of cell boundary coordinates in $\alpha$ -direction. Cell "I" is bounded by AKB(I-1) and ADB(I), (Radians)
BKB(I)	Array of cell boundary coordinates in $\beta$ -direction. Cell "I" is bounded by BKB(I-1) and BKB(I), (Radians)
PKB(I)	Array of cell boundary coordinates in $\phi$ -direction. Cell "I" is bounded by PKB(I-1) and PKB(I), (Radians)
DAKB(I)	Array of cell widths in $\alpha$ -direction (Radians)
DBKB(I)	Array of cell widths in $\beta$ -direction (Radians)
DPKB(I)	Array of cell widths in $\phi$ -direction (Radians)
BKV(I),	Arrays of vertex $\beta$ and $\phi$ - coordinates for the four corners
PKV(I)	of each stick. (Radians)
CJA(I)	Array of $J_{\alpha}$ current density components ( $ABAMPS/cm^2$ ). These density components are defined at the points $(AKB(K), 1/4 \sum_I BKV(I), 1/4 \sum_I PKV(I))$

BV, PV       $\beta$  and  $\phi$ -coordinates of vertex (Radians)  
 AKC(I)      Array of cell centered  $\alpha$ -coordinates (Radians)  
                $AKC(I) = 1/2(AKB(I) + AKB(I-1))$   
 CJB(I),      Arrays of  $\beta$  and  $\phi$  current density components. Defined at  
 CJP(I)      points (AKC(I), BV, PV). (ABAMPS/cm<sup>2</sup>)

## Appendix D

### DERIVATION OF LAGRANGEAN VOLUME ELEMENT

The derivation of Lagrangean volume element (derivation supplied to MDAC by Bill White of MRC) is given below (see also Figure D-1):

Volume of  $\alpha\beta\phi$  Lagrangean Element

$$V = \iiint h_\alpha h_\beta h_\phi d\alpha d\beta d\phi = \iiint R^2 \sin\theta dR d\theta d\phi$$

$$V = \iiint R^2 \sin\theta dR d\theta d\phi$$

$$= \Delta\phi \int_{\theta_1}^{\theta_2} d\theta \sin\theta \int_{R_e \sqrt{\frac{\cos\theta}{\cos\alpha_1}}}^{R_e \frac{\sin^2\theta}{\sin^2\beta_1}} dR R^2 + \Delta\phi \int_{\theta_2}^{\theta_3} d\theta \sin\theta \int_{R_e \sqrt{\frac{\cos\theta}{\cos\alpha_1}}}^{R_e \sqrt{\frac{\cos\theta}{\cos\alpha_2}}} dR R^2$$

$$+ \Delta\phi \int_{\theta_3}^{\theta_4} d\theta \sin\theta \int_{R_e \frac{\sin^2\theta}{\sin^2\beta_2}}^{R_e \sqrt{\frac{\cos\theta}{\cos\alpha_2}}} dR R^2$$

$$= \frac{\Delta\phi R_e^3}{3} \int_{\theta_1}^{\theta_2} d\theta \sin\theta \left( \left( \frac{\sin^2\theta}{\sin^2\beta_1} \right)^3 - \left( \frac{\cos\theta}{\cos\alpha_1} \right)^{3/2} \right)$$

$$+ \frac{\Delta\phi R_e^3}{3} \int_{\theta_2}^{\theta_3} d\theta \sin\theta \left( \left( \frac{\cos\theta}{\cos\alpha_2} \right)^{3/2} - \left( \frac{\cos\theta}{\cos\alpha_1} \right)^{3/2} \right)$$

$$\begin{aligned}
& + \frac{\Delta\phi R_e^3}{3} \int_{\theta_3}^{\theta_4} d\theta \sin\theta \left( \left( \frac{\cos\theta}{\cos\alpha_2} \right)^{3/2} - \left( \frac{\sin^2\theta}{\sin^2\beta_2} \right)^3 \right) \\
& = \frac{\Delta\phi R_e^3}{3} \left( \int_{\theta_1}^{\theta_2} d\theta \sin\theta \left( \frac{\sin^2\theta}{\sin^2\beta_1} \right)^3 - \int_{\theta_1}^{\theta_3} d\theta \sin\theta \left( \frac{\cos\theta}{\cos\alpha_1} \right)^{3/2} \right. \\
& \quad \left. + \int_{\theta_2}^{\theta_4} d\theta \sin\theta \left( \frac{\cos\theta}{\cos\alpha_2} \right)^{3/2} - \int_{\theta_3}^{\theta_4} d\theta \sin\theta \left( \frac{\sin^2\theta}{\sin^2\beta_2} \right)^3 \right) \\
& = \frac{\Delta\phi R_e^3}{3} \left\{ \frac{1}{\sin^6\beta_1} \left( -\cos\theta + \cos^3\theta - \frac{3}{5}\cos^5\theta + \frac{1}{7}\cos^7\theta \right) \right|_{\theta_1}^{\theta_2} \\
& \quad + \frac{2}{5} \left( \frac{\cos\theta}{\cos\alpha_1} \right)^{3/2} \cos\theta \Big|_{\theta_1}^{\theta_3} - \frac{2}{5} \left( \frac{\cos\theta}{\cos\alpha_2} \right)^{3/2} \cos\theta \Big|_{\theta_2}^{\theta_4} \\
& \quad + \frac{1}{\sin^6\beta_2} \left( \cos\theta - \cos^3\theta + \frac{3}{5}\cos^5\theta - \frac{1}{7}\cos^7\theta \right) \Big|_{\theta_3}^{\theta_4} \right\}
\end{aligned}$$

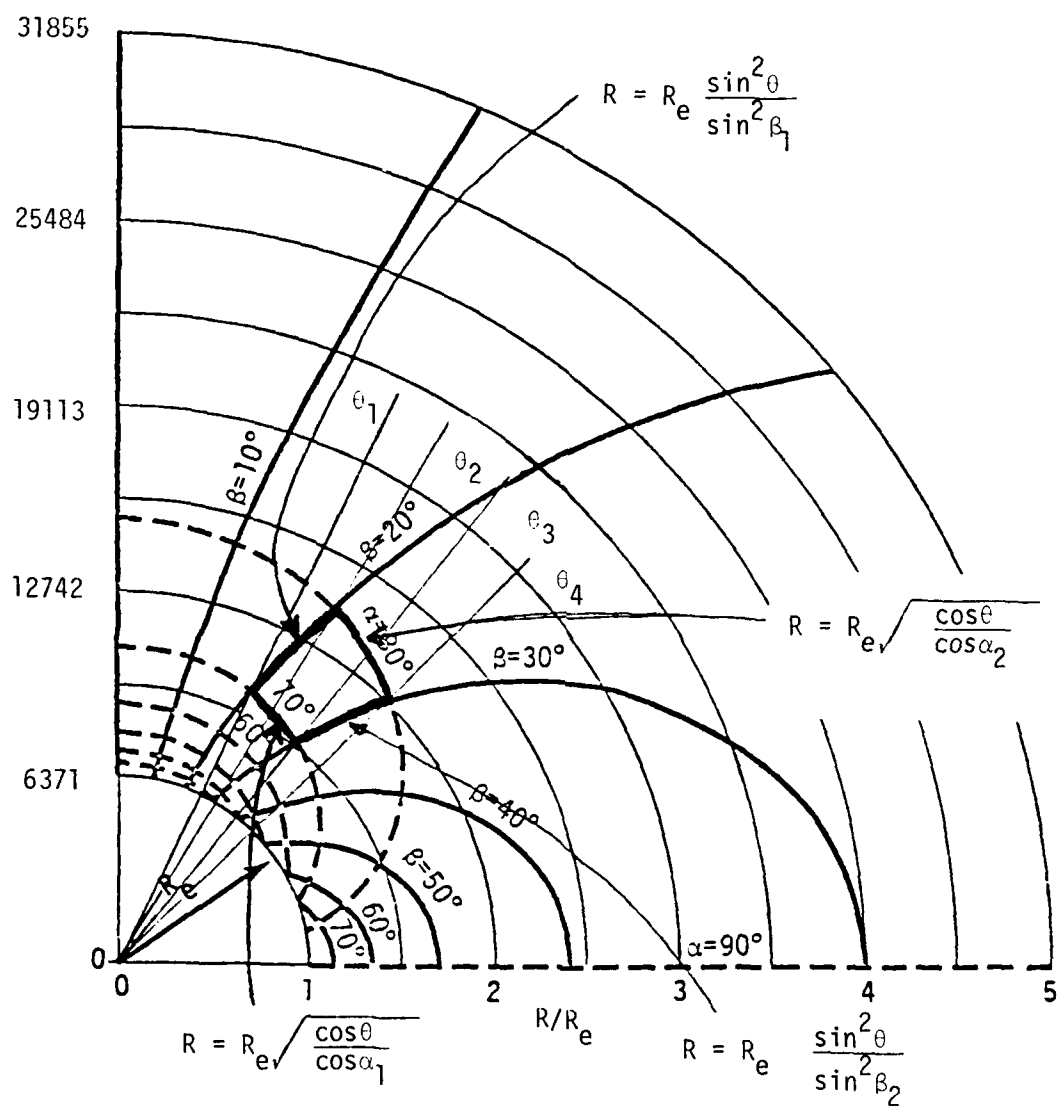


Figure D-1. The  $(\alpha, \beta)$  coordinates for the field-aligned dipole coordinate system far from the earth.

## DISTRIBUTION LIST

### DEPARTMENT OF DEFENSE

Assistant Secretary of Defense  
Comm., Cmd. Cont. & Intell.  
ATTN: Dir. of Intelligence Systems,  
J. Babcock  
ATTN: C3IST&CCS, M. Epstein

Assistant to the Secretary of Defense  
Atomic Energy  
ATTN: Executive Assistant

Defense Advanced Rsch. Proj. Agency  
ATTN: TIO

Defense Communications Agency  
ATTN: Code 101B  
ATTN: Code 205  
ATTN: Code 480, F. Dieter

Defense Communications Engineer Center  
ATTN: Code R123  
ATTN: Code R410, R. Craighill

Defense Nuclear Agency  
ATTN: DDST  
3 cy ATTN: RAAE  
4 cy ATTN: TITL

Defense Technical Information Center  
12 cy ATTN: DD

Field Command  
Defense Nuclear Agency  
ATTN: FCPR

Field Command  
Defense Nuclear Agency  
Livermore Division  
ATTN: FCPRL

Interservice Nuclear Weapons School  
ATTN: TTV

Joint Chiefs of Staff  
ATTN: J-3, WWMCCS Evaluation Office

Undersecretary of Defense for Rsch. & Engrg.  
ATTN: Strategic & Space Systems (OS)

WWMCCS System Engineering Org.  
ATTN: R. Crawford

DEPARTMENT OF THE ARMY

Atmospheric Sciences Laboratory  
U.S. Army Electronics R&D Command  
ATTN: DELAS-EO, F. Niles

BMD Advanced Technology Center  
Department of the Army  
ATTN: ATC-R, D. Russ  
ATTN: ATC-T, M. Capps  
ATTN: ATC-O, W. Davies

BMD Systems Command  
Department of the Army  
ATTN: BMDSC-HW

### DEPARTMENT OF THE ARMY (Continued)

Harry Diamond Laboratories  
Department of the Army  
ATTN: DELHD-N-P  
ATTN: DELHD-N-P, F. Wimenitz  
ATTN: DELHD-I-TL, M. Weiner

U.S. Army Materiel Dev. & Readiness Cmd.  
ATTN: DRCLDC, J. Bender

U.S. Army Missile Intelligence Agency  
ATTN: J. Gamble

U.S. Army Nuclear & Chemical Agency  
ATTN: Library

U.S. Army Satellite Comm. Agency  
ATTN: Document Control

U.S. Army TRADOC Systems Analysis Activity  
ATTN: ATAA-PL

### DEPARTMENT OF THE NAVY

Naval Electronic Systems Command  
ATTN: PME 117-211, B. Kruger  
ATTN: Code 501A  
ATTN: PME 117-2013, G. Burnhart  
ATTN: PME 117-20

Naval Research Laboratory  
ATTN: Code 6700, T. Coffey  
ATTN: Code 6780, S. Ossakow

Naval Surface Weapons Center  
ATTN: Code F31

Office of Naval Research  
ATTN: Code 465

Strategic Systems Project Office  
Department of the Navy  
ATTN: NSP-2722, F. Wimberly  
ATTN: NSP-43

### DEPARTMENT OF THE AIR FORCE

Air Force Avionics Laboratory  
ATTN: AAD, W. Hunt  
ATTN: AAD, A. Johnson

Air Force Geophysics Laboratory  
ATTN: OPR, A. Stair  
ATTN: OPR, H. Gardiner  
ATTN: PHI, J. Buchau  
ATTN: PHP, J. Mullen

Air Force Weapons Laboratory, AFSC  
ATTN: DYC  
ATTN: SUL

Deputy Chief of Staff  
Research, Development, & Acq.  
Department of the Air Force  
ATTN: AFRDQ

DEPARTMENT OF THE AIR FORCE (Continued)

Headquarters Space Division  
Air Force Systems Command  
ATTN: SKA, M. Clavin

Headquarters Space Division  
Air Force Systems Command  
ATTN: SZJ, W. Mercer  
ATTN: SZJ

Strategic Air Command  
Department of the Air Force  
ATTN: XPFS  
ATTN: NRT

DEPARTMENT OF ENERGY CONTRACTORS

Lawrence Livermore Laboratory  
ATTN: Document Control for L-31, R. Hager  
ATTN: Document Control for L-389, R. Ott

Los Alamos Scientific Laboratory  
ATTN: Document Control for E. Jones  
ATTN: Document Control for D. Simons  
ATTN: Document Control for MS 664, J. Zinn

Sandia Laboratories  
ATTN: Document Control for Org. 4241,  
T. Wright  
ATTN: Document Control for Org. 1250,  
W. Brown

EG&G, Inc.  
Los Alamos Division  
ATTN: Document Control for J. Colvin  
ATTN: Document Control for D. Wright

OTHER GOVERNMENT AGENCY

Institute for Telecommunications Sciences  
National Telecommunications & Info. Admin.  
ATTN: W. Utlaut

DEPARTMENT OF DEFENSE CONTRACTORS

Aerospace Corp.  
ATTN: N. Stockwell  
ATTN: V. Josephson  
ATTN: D. Olsen

Berkeley Research Associates, Inc.  
ATTN: J. Workman

Charles Stark Draper Lab., Inc.  
ATTN: D. Cox  
ATTN: J. Gilmore

ESL, Inc.  
ATTN: G. Prebble  
ATTN: T. Marshall

General Electric Co.  
ATTN: M. Bortner

General Electric Company-TEMPO  
ATTN: W. Knapp  
ATTN: W. McNamara  
ATTN: T. Stevens  
ATTN: DAGIAC  
ATTN: M. Stanton

DEPARTMENT OF DEFENSE CONTRACTORS (Continued)

General Research Corp.  
ATTN: J. Ise, Jr.  
ATTN: J. Garbarino

GTE Sylvania, Inc.  
ATTN: M. Cross

HSS, Inc.  
ATTN: D. Hansen

Institute for Defense Analyses  
ATTN: E. Bauer

JAYCOR  
ATTN: S. Goldman

Johns Hopkins University  
ATTN: T. Potemra

Kaman Sciences Corp.  
ATTN: T. Meagher

Lockheed Missiles & Space Co., Inc.  
ATTN: D. Churchill

M.I.T. Lincoln Lab.  
ATTN: D. Towle

Martin Marietta Corp.  
ATTN: R. Heffner

McDonnell Douglas Corp.  
ATTN: G. Mroz  
ATTN: R. Halprin  
ATTN: W. Olson  
ATTN: K. Pfitzer  
ATTN: S. Schneider

Mission Research Corp.  
ATTN: D. Sowle  
ATTN: R. Bogusch  
ATTN: D. Sappenfield  
ATTN: F. Fajen  
ATTN: R. Kilb  
ATTN: S. Gutsche  
ATTN: R. Hendrick

Mitre Corp.  
ATTN: W. Hall  
ATTN: J. Wheeler  
ATTN: W. Foster

Photometrics, Inc.  
ATTN: I. Kofsky

Physical Dynamics, Inc.  
ATTN: A. Thompson

Physical Dynamics, Inc.  
ATTN: F. Fremouw

R&D Associates  
ATTN: C. MacDonald  
ATTN: W. Karzas  
ATTN: B. Gabbard  
ATTN: F. Gilmore  
ATTN: R. Lelevier



DEPARTMENT OF DEFENSE CONTRACTORS (Continued)

Rand Corp.

ATTN: E. Bedrozian  
ATTN: C. Crain

Science Applications, Inc.

ATTN: D. Hamlin  
ATTN: J. McDougall  
ATTN: L. Linson  
ATTN: D. Sachs

Science Applications, Inc.

ATTN: D. Divis

Science Applications, Inc.

ATTN: J. Cockayne

Visidyne, Inc.

ATTN: C. Humphrey  
ATTN: J. Carpenter

DEPARTMENT OF DEFENSE CONTRACTORS (Continued)

SRI International

ATTN: M. Baron  
ATTN: C. Rino  
ATTN: G. Smith  
ATTN: R. Leadabrand  
ATTN: W. Chesnut  
ATTN: W. Jaye

Technology International Corp.

ATTN: W. Boquist

Teledyne Brown Engineering

ATTN: R. Deliberis

TRW Defense & Space Sys. Group

ATTN: R. Plebuch